A 3-D crustal shear wave velocity model and Moho map below the Semail Ophiolite, eastern Arabia

C. Weidle, L. Wiesenberg, A. El-Sharkawy, F. Krüger, A. Scharf, Philippe Agard, T. Meier

▶ **To cite this version:**

C. Weidle, L. Wiesenberg, A. El-Sharkawy, F. Krüger, A. Scharf, et al.. A 3-D crustal shear wave velocity model and Moho map below the Semail Ophiolite, eastern Arabia. Geophysical Journal International, 2022, 231, pp.817-834. 10.1093/gji/ggac223 . insu-03747375

HAL Id: insu-03747375
https://insu.hal.science/insu-03747375

Submitted on 16 Mar 2023

HAL is a multi-disciplinary open access archive for the deposit and dissemination of scientific research documents, whether they are published or not. The documents may come from teaching and research institutions in France or abroad, or from public or private research centers.

L'archive ouverte pluridisciplinaire **HAL**, est destinée au dépôt et à la diffusion de documents scientifiques de niveau recherche, publiés ou non, émanant des établissements d'enseignement et de recherche français ou étrangers, des laboratoires publics ou privés.

Geophysical Journal International

Geophys. J. Int. (2022) **231,** 817–834
Advance Access publication 2022 June 16
GJI Seismology

https://doi.org/10.1093/gji/ggac223

A 3-D crustal shear wave velocity model and Moho map below the Semail Ophiolite, eastern Arabia

C. Weidle [1], L. Wiesenberg [1], A. El-Sharkawy,[1,2,3] F. Krüger,[4] A. Scharf,[5] P. Agard[6] and T. Meier[1]

[1] *Kiel University, Institute of Geosciences, Otto-Hahn-Platz* 1, 24118 *Kiel, Germany. E-mail: christian.weidle@ifg.uni-kiel.de*
[2] *National Research Institute of Astronomy and Geophysics (NRIAG),* 11421 *Helwan Cairo, Egypt*
[3] *Faculty of Earth Sciences, Beni-Suef University, Beni-Suef, Egypt*
[4] *University of Potsdam, Institute of Geosciences, Karl-Liebknecht-Str.* 24-25, 14476 *Potsdam, Germany*
[5] *Department of Earth Sciences, College of Science, Sultan Qaboos University, PO Box* 36, *PC* 123, *Al-Khod, Muscat, Sultanate of Oman*
[6] *Sorbonne Université, CNRS-INSU, Institut des Sciences de la Terre Paris, ISTeP UMR* 7193, 75005 *Paris, France*

Accepted 2022 June 14. Received 2022 June 9; in original form 2021 October 21

SUMMARY

The Semail Ophiolite in eastern Arabia is the largest and best-exposed slice of oceanic lithosphere on land. Detailed knowledge of the tectonic evolution of the shallow crust, in particular during and after ophiolite obduction in Late Cretaceous times is contrasted by few constraints on physical and compositional properties of the middle and lower continental crust below the obducted units. The role of inherited, pre-obduction crustal architecture remains therefore unaccounted for in our understanding of crustal evolution and the present-day geology. Based on seismological data acquired during a 27-month campaign in northern Oman, Ambient Seismic Noise Tomography and Receiver Function analysis provide for the first time a 3-D radially anisotropic shear wave velocity (V_S) model and a consistent Moho map below the iconic Semail Ophiolite. The model highlights deep crustal boundaries that segment the eastern Arabian basement in two distinct units. The previously undescribed Western Jabal Akhdar Zone separates Arabian crust with typical continental properties and a thickness of ∼40–45 km in the northwest from a compositionally different terrane in the southeast that is interpreted as a terrane accreted during the Pan-African orogeny in Neoproterozoic times. East of the Ibra Zone, another deep crustal boundary, crustal thickness decreases to 30–35 km and very high lower crustal V_S suggest large-scale mafic intrusions into, and possible underplating of the Arabian continental crust that occurred most likely during Permian breakup of Pangea. Mafic reworking is sharply bounded by the (upper crustal) Semail Gap Fault Zone, northwest of which no such high velocities are found in the crust. Topography of the Oman Mountains is supported by a mild crustal root and Moho depth below the highest topography, the Jabal Akhdar Dome, is ∼42 km. Radial anisotropy is robustly resolved in the upper crust and aids in discriminating dipping allochthonous units from autochthonous sedimentary rocks that are indistinguishable by isotropic V_S alone. Lateral thickness variations of the ophiolite highlight the Haylayn Ophiolite Massif on the northern flank of Jabal Akhdar Dome and the Hawasina Window as the deepest reaching unit. Ophiolite thickness is ∼10 km in the southern and northern massifs, and ≤5 km elsewhere.

Key words: Composition and structure of the continental crust; Asia; Body waves; Seismic anisotropy; Seismic tomography; Surface waves and free oscillations.

1 INTRODUCTION

The northeastern continental margin of Arabia, with the world's largest and best preserved exposure of oceanic lithosphere—the Semail Ophiolite—has been a focal point of geoscientific research for more than five decades, most notably on creation of oceanic lithosphere, subduction initiation, continental subduction and exhumation, and many more (e.g. Glennie *et al.* 1974; Hacker *et al.* 1996; Nicolas *et al.* 1996, 2000; Agard *et al.* 2007). Together with subsurface studies in interior Oman, those studies provide a detailed picture of the present-day geology (Fig. 1a), the evolution of the shallow crust, as well as a thorough framework for the

© The Author(s) 2022. Published by Oxford University Press on behalf of The Royal Astronomical Society.

Downloaded from https://academic.oup.com/gji/article/231/2/817/6609440 by CNRS user on 16 March 2023

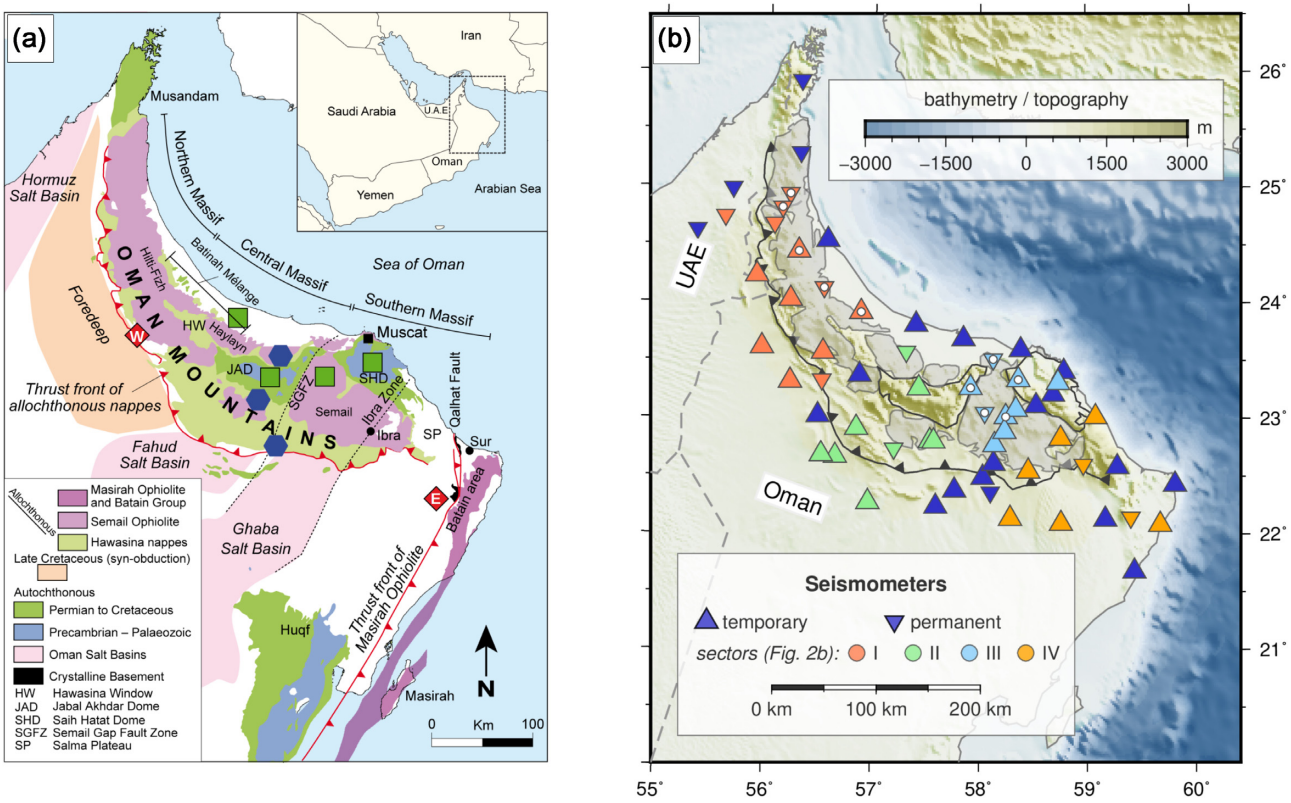

Figure 1. (a) Tectonic overview map, modified after Forbes *et al.* (2010). Locations of 1-D models in Fig. 4 (red diamonds), Fig. 5 (green squares), and Fig. 7 (blue hexagons). (b) Overview map of temporary (triangles) and permanent (inverted triangles) seismic stations used in this study. Colours and white dots refer to Fig. 2(b).

geodynamics of obduction of the Semail Ophiolite. At the same time, little is known about the geological and physical properties, and lateral variations therein, of the middle and lower crust because the crystalline basement of eastern Arabia is, except from few isolated locations, covered by a thick cover of Neoproterozoic and Phanerozoic sedimentary rocks. Obduction of the Semail Ophiolite during the Late Cretaceous was preceded by at least two major tectonic events—the Neoproterozoic assembly of Gondwana and the Permo-Triassic breakup of Pangea—and these events must have left their imprint deep in the eastern Arabian crust. However, the role and significance of previous tectonic episodes on obduction dynamics and geometry is unknown.

Based on passive seismological data acquired during a temporary deployment, we present and discuss the construction of a 3-D crustal-scale model of radially anisotropic shear wave velocities for eastern Arabia from ambient seismic noise tomography (ANT). A thorough evaluation of the inversion parameters and resolution capabilities addresses the resolution of Moho depths and radial anisotropy in particular. The model is complemented by a separate analysis of receiver functions (RF) which establishes independent constraints on crustal thickness in the study area. We finally combine ANT and RF results to obtain a consistent Moho map which also allows us to identify lateral variations in V_P/V_S ratios.

1.1 Geology and tectonics of eastern Arabia

Prior to obduction, the palaeogeography of eastern Arabia was comparable to the present-day, with continental margins in the northeast and east, adjacent to the Neo-Tethys (today Sea of Oman) and the Indian Ocean, respectively (e.g. Blendinger *et al.* 1990). At $\gtrsim$104Ma, an intra-oceanic, northerly dipping subduction zone formed within the Neo-Tethys Ocean (e.g. Guilmette *et al.* 2018; Tavani *et al.* 2020). Rollback and rotation of the subduction trench towards Arabia resulted in extension within the upper plate and formation of a spreading centre and new oceanic lithosphere at ∼96 Ma—the future Semail Ophiolite (e.g. Rioux *et al.* 2016). Coeval with its formation, the hot oceanic lithosphere thrusted above subducting oceanic lithosphere of the Neo-Tethys Ocean and on an adjacent deep-ocean sedimentary basin (Hawasina Basin). As the distal Arabian continental lithosphere was dragged into the subduction zone, the Semail Ophiolite was finally emplaced together with underlying nappes from the Hawasina Basin onto the Arabian continent (e.g. Agard *et al.* 2010). Today, the allochthonous nappes of obducted Hawasina units and overlying Semail Ophiolite (Fig. 1a) cover almost the entire Oman Mountains, a ∼500 km long, arcuate shaped, coast parallel mountain belt with a peak elevation of 3000 m (Fig. 1b). Within the Oman Mountains, Neoproterozoic to Cretaceous exposures of sedimentary rocks in the Jabal Akhdar (JAD) and Saih Hatat Domes (SHD, Fig. 1a) provide insight into the pre-obduction tectonic history of the east Arabian continental margin.

In Neoproterozoic times, eastern Arabia was accreted to the Arabian–Nubian shield as part of Pan-African orogenic events in the assembly of Gondwana (e.g. Allen 2007; Whitehouse *et al.* 2016). Several large-scale tectonic elements in Oman suggest that terrane accretion, as well as post-orogenic transtension occurred along NNE-striking faults and formed NNE-oriented salt basins and differential vertical motion of the Huqf area (Fig. 1a, Allen

Downloaded from https://academic.oup.com/gji/article/231/2/817/6609440 by CNRS user on 16 March 2023

2007). A major extensional phase during the late Palaeozoic led to the breakup of—by then supercontinent—Pangea and formation of the Neo-Tethys Ocean and Indian Ocean margins. The northeastern corner of Arabia was located close to the triple junction and vast amounts of mafics in the SHD are evidence of massive volcanism during plate breakup (e.g. Chauvet *et al.* 2009). Notably, the JAD was only minorly affected by such mafics (e.g. Blendinger *et al.* 1990), which suggests that the Semail Gap Fault Zone (SGFZ, Fig. 1a), a major fault at the eastern margin of the JAD, acted as a structural boundary at the time (e.g. Scharf *et al.* 2019; Ninkabou *et al.* 2021). After breakup of Pangea, most of Arabia became a passive platform until the onset of convergence on the Neo-Tethys margin in mid-Cretaceous times that culminated in obduction of the Semail Ophiolite. About 15–20 Myr later, the northward passage of India led to thrusting of deep-ocean complexes of the Batain Group and the Masirah Ophiolite along the eastern Arabian margin (Fig. 1a, e.g. Schreurs & Immenhauser 1999), mostly offshore and onshore only in a narrow coastal zone. More details on the geology and tectonics of eastern Arabia were recently compiled by Scharf *et al.* (2021).

1.2 Crustal structure in northern Oman

Geophysical, primarily gravity data across northern Oman have established density models that reconcile surface geology with the strong density contrasts between autochthonous (sedimentary) and allochthonous (mostly igneous) rocks. However, in absence of additional constraints, a homogeneous density distribution in the middle to lower crust has been assumed in all those models and lateral structural variations, as well as the depth of the crust–mantle boundary remained often ill- or unconstrained (e.g. Manghnani & Coleman 1981; Ravaut *et al.* 1997; Al-Lazki *et al.* 2002). Similarly, lateral changes in ophiolite thickness from 2 to 10 km were inferred from gravity data, but both geometry and density of the ophiolite bodies remain inconclusive due to lacking geometrical constraints at depth from independent, for example seismic data (e.g. Ravaut *et al.* 1997). A single comprehensive, crustal-scale geophysical profile combines gravity with seismic and borehole data across the Jabal Akhdar Dome and provides a reference model of the crust in northern Oman (Al-Lazki *et al.* 2002). This model shows that ophiolite thickness south of the dome is negligible (<1 km) but amounts to ∼5 km on the northern flank. Autochthonous Permian to Cretaceous sedimentary rocks extend to 8–10 km depth within and south of the dome and are thinner northwards. The topography of the dome is sustained by a crustal root where the Moho is ∼10 km deeper than south and north of the dome. More recently, localized estimates of Moho depth across northern Oman confirm a 36–48-km-thick crust below northern Oman (Al-Hashmi *et al.* 2011) but these observations are too sparse to laterally resolve crustal thickening below the topography over the entire mountain belt. They also do not reveal a regional trend in crustal thickness which is in strong contrast to global (CRUST1.0, Laske *et al.* 2013), as well as regional, gravity based Moho maps (Jiménez-Munt *et al.* 2012; Mechie *et al.* 2013). The latter suggest a shallowing of the Moho from ∼40 to 45 km in interior eastern Arabia to ∼30 km at the northeastern coast of Oman.

These inconsistencies and largely unknown properties of the middle and lower continental crust leave numerous open questions on the evolution of the eastern Arabian crust, the geometry and dynamics of obduction and related lateral changes in surface geology unanswered. These questions include, but are not limited to, the eastern limit of the obducted units, the (north)western and (south)eastern limits of the Jabal Akhdar and Saih Hatat Domes, respectively, lateral thickness variations in the ophiolite massifs, or the geometry and mechanisms forming the Hawasina Window (HW, Fig. 1a). Thus, there is a need to constrain the structural properties of the Arabian continental crust in general but especially below the ophiolite to propel our understanding of the geodynamics of eastern Arabia from the Proterozoic to Present.

2 DATA SET AND METHODS

We operated a temporary network of 40 broad-band seismometers for a period of 27 months across the Oman Mountains (Fig. 1b, Weidle *et al.* 2013). The dataset is complemented by recordings of stations from the permanent Oman Seismic Network, the Dubai Seismic Network (UAE) and the Global Seismographic Network station UOSS in Sharjah (UAE). The network covered an area of ∼500 km by 150 km, consisted of 40 temporary and 14 permanent broadband seismometers and recorded continuous seismic waveforms from October 2013 to February 2016 (a complete station list is appended in Table A1).

2.1 Receiver functions

We estimate sediment and total crustal thickness from interpretation of P- and S-type receiver functions (RF), both well established and widely used methods to image velocity discontinuities at depth (e.g. Vinnik 1977; Langston 1979; Kind *et al.* 1995; Yuan *et al.* 2006; Knapmeyer-Endrun *et al.* 2014). We analyse 769 teleseismic events with magnitudes ≥5.5 during the deployment period of the temporary network (Fig. 2a). Most events with magnitudes ≥6 occurred at N to ESE backazimuths. Events in the azimuth range SE to W are mostly at the lower magnitude end and the estimated RF from those events have often a poor signal-to-noise ratio. For P-RF's, the *P*-to-*S*-wave conversion at a discontinuity, events within an epicentral distance of 30–100° are selected. PKP-waves, which are observable at epicentral distances larger than 150° were not investigated due to poor signal to noise ratio. For S-RF's, the conversion of *S*-to-*P* waves, *S* waves from events between 55° and 85°, and SKS waves from events up to epicentral distances of 120° were analysed (Yuan *et al.* 2006).

Raw waveforms were lowpass filtered at 5 Hz and rotated into a LQT ray coordinate system based on theoretical backazimuths and incidence angles predicted by the IASP91 velocity model (Kennett & Engdahl 1991). For P-RF, we deconvolve the *Q*- and *T*-component with the *P* wave on the L-component. For S-RF, theoretical incidence angles for the Sp Moho conversion (L-component) and direct *S* wave (Q-component) are used to deconvolve the L- with the Q-component. Deconvolution is performed in a window of 100 s length with a time domain inverse filter generated from the P-wave on the L-component (P-RF) or the *S* wave on the Q-component (S-RF, Berkhout 1977; Kind *et al.* 1995). RFs with a low signal to noise ratio were removed. Our data set contains 2293 P-RF and 736 S-RF, up to 95 and 42 individual RF observations per station for P-RF and S-RF, respectively. After moveout correction to account for the varying slowness of the individual RF, a single RF stack is calculated for each seismic station. Finally, a zero-phase Butterworth low-pass filter at 2 s corner period was applied before we manually picked delay times of converted phases (4 s low-pass corner period for S-RF).

Downloaded from https://academic.oup.com/gji/article/231/2/817/6609440 by CNRS user on 16 March 2023

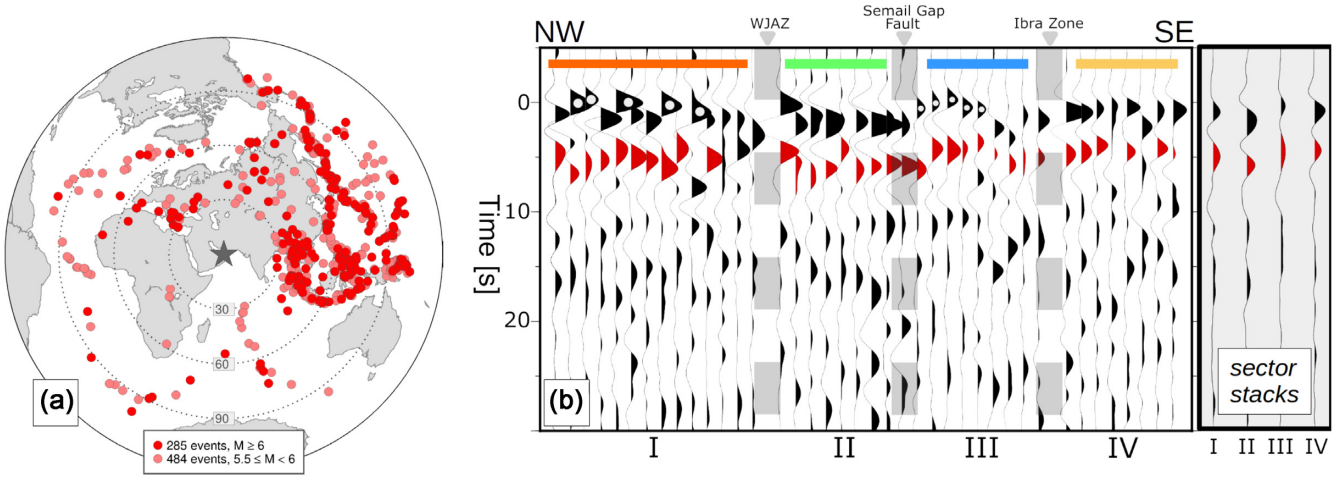

Figure 2. Receiver function section through network. (a) teleseismic events used for receiver function analysis. (b) NW-SE profile of stacked P-Receiver Functions, sector colours and white dots in earliest conversion refer to Fig. 1(b).

In almost all P-RF stacks a distinct Moho conversion can be identified at 3.5–5 s delay time (Fig. 2b), preceded in many cases by another, equally strong conversion signal at 1.4–2 s with the same polarity. The latter conversion is particularly consistent in the southern foreland and the Central Oman Mountains, whereas earlier arrivals at $\leq$1 s are observed in the Eastern Oman Mountains. Some sites have very small delay times, the majority of these are located on ophiolite nappes on the north flank of the mountain belt and between the Jabal Akhdar and Saih Hatat Domes (marked by 'white dots' in Figs 1b and 2b).

The number of S-RF per station is considerably lower, on average only 15 individual RFs could be obtained due to the requirement of a high signal-to-noise ratio for direct SV or SKS phases. Despite the fewer data in S-RF, Moho delay times are very consistent with those derived from P-RF (Fig. 3). Delay times are overall larger in the northwestern mountain belt than east of the Saih Hatat Dome and the southern foreland.

We also applied the grid search method of Zhu & Kanamori (2000) (ZK) and stacked direct conversions and crustal multiples, calculated a semblance coefficient for each stack and used well constrained overall maxima in the resulting semblance maps to obtain crustal thickness and crust-average V_P/V_S velocity ratios below each seismic station. Again, we stacked the P-RF for each individual station first in bins of 0.1 s/deg width (0.15 s deg^{-1} for S-RF). The individual traces were band-pass filtered with zero-phase Butterworth band-pass filters of 3rd order in the pass-bands 4–30 s and 8–32 s to account for the lower dominant frequencies of the crustal multiples. Our modified ZK analysis uses the average crustal V_S velocities obtained from ambient noise tomography (see below) as fixed velocity (not *Vp* as in the original version of ZK). For S-RFs a similar grid search technique was used (Wittlinger *et al.* 2009) but we did not use P-RF and S-RF together because, for a thick crust, the respective multiples illuminate different areas around each station.

2.2 Ambient noise surface wave tomography

Ambient noise surface wave tomography (ANT) is used to derive a 3-D radially anisotropic shear wave velocity model of the crust in the study region. Ambient noise cross-correlation functions are calculated for all station pairs within the network area by cross-correlating continuous seismic waveforms in daily data windows. Prior to the cross-correlation, the waveforms are normalized in the time domain by removing a running absolute mean amplitude of bandpass filtered data, and spectrally whitened (Bensen *et al.* 2007). We measure surface wave phase velocity dispersion curves for fundamental mode Rayleigh and Love waves in the period range 2–40 s by fitting the phase spectrum of the causal, symmetric part of the cross-correlation functions, as described in detail by Wiesenberg *et al.* (2022). The dataset for tomographic inversion contains 400–900 paths in the period range 6–25 s for Rayleigh, and 200–550 paths in the period range 5–20 s for Love waves. At periods longer than 25 s, the number of dispersion curves decreases strongly for Love waves. Azimuthal path coverage is best in the Central and Eastern Oman Mountains and resolution tests suggest that velocity anomalies of ~30 km can be resolved in most parts of the study region (Wiesenberg *et al.* 2022).

Azimuthally anisotropic phase velocity maps are then calculated by tomographic inversion of the phase velocity dispersion curves at periods 2–30 s (Deschamps *et al.* 2008; Darbyshire & Lebedev 2009; Wiesenberg *et al.* 2022). They show a good match to surface geology with high phase velocities in the mountain belt and the tectonic windows and low velocities in the foreland at periods up to ~7 s. At larger periods, the anomaly pattern changes to a west–east contrast with higher phase velocities in the east and below the tectonic windows. Details and interpretation of phase velocity maps and azimuthal anisotropy are discussed in Wiesenberg *et al.* (2022).

We extract local Rayleigh and Love wave dispersion curves from the isotropic component of Rayleigh and Love wave phase velocity maps at each point of a 10 km by 10 km grid across the study region and apply a probabilistic inversion based on the Particle Swarm Optimization to invert for local, radially anisotropic 1-D profiles of shear wave velocity as function of depth (El-Sharkawy *et al.* 2020). In extension to (El-Sharkawy *et al.* 2020), we account for radial anisotropy by inverting Rayleigh and Love wave dispersion curves for perturbations in V_{SV} and V_{SH} simultaneously.

The inversion uses a simple starting model with a constant shear wave velocity (2.9 km s^{-1}) in the entire crust (inset Fig. 4b). The only parameter that varies across all starting models in the study area is the Moho depth, which we select for each local inversion point from the closest point in the global crustal model CRUST1.0 (Laske *et al.* 2013). We deliberately avoid converting RF–Moho conversion times as constraints for the ANT inversion. This has the benefit that

Downloaded from https://academic.oup.com/gji/article/231/2/817/6609440 by CNRS user on 16 March 2023

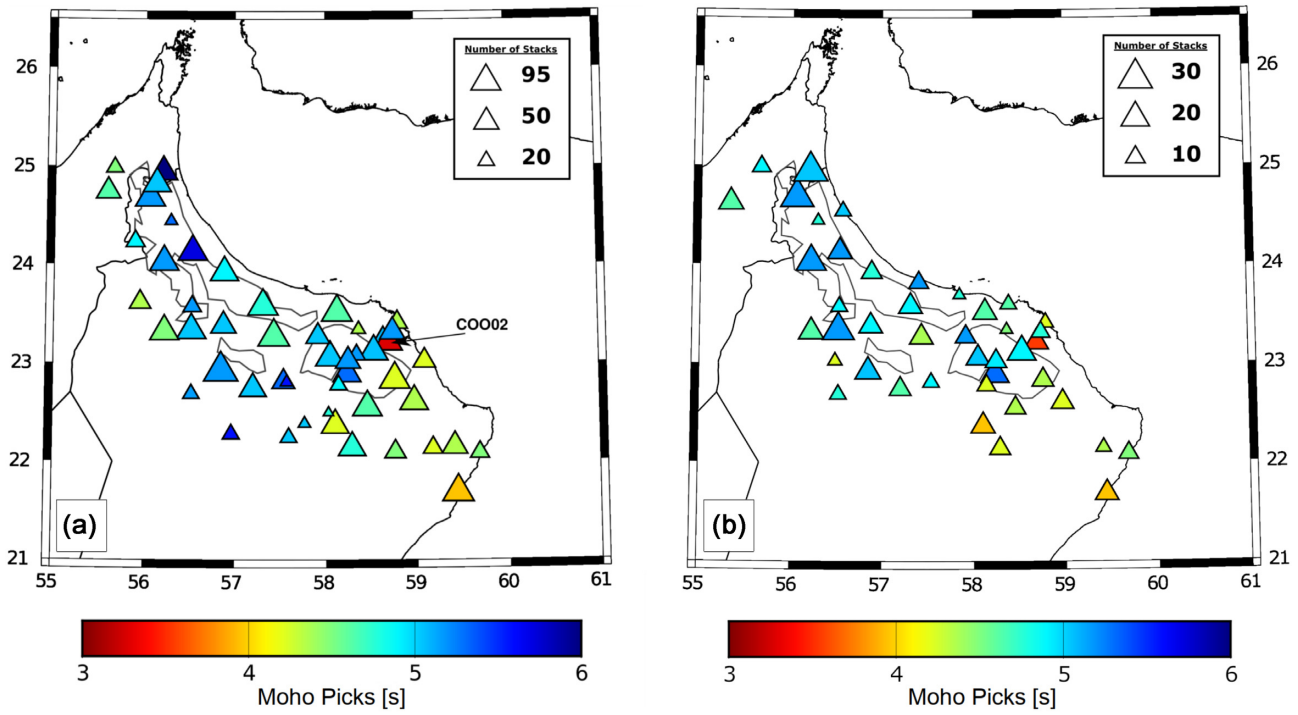

Figure 3. Moho delay times from (a) P- and (b) S-receiver functions. Size of triangle shows number of individual RFs per station.

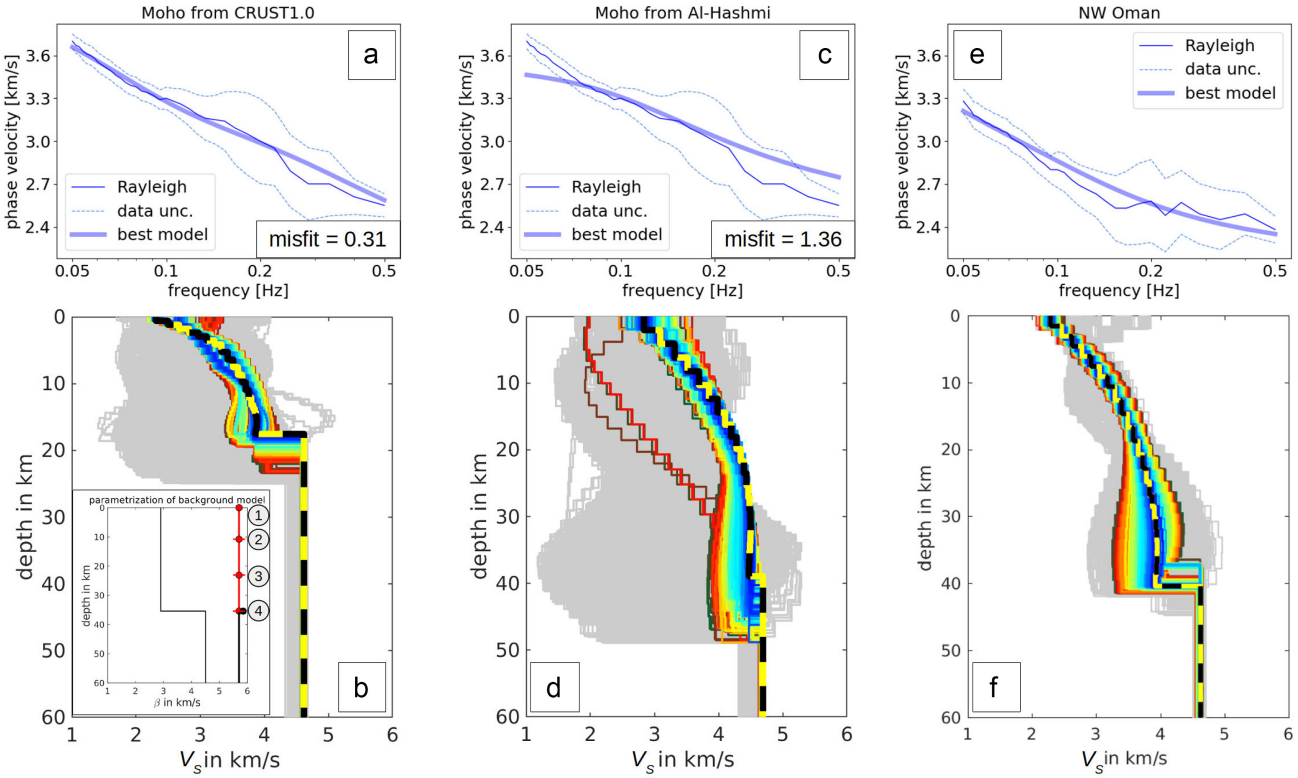

Figure 4. Inversion of local Rayleigh dispersion curve for Moho sensitivity at two model points (shown as red diamonds in Fig 1a). (a, c, e): Rayleigh local dispersion curve (thin solid), standard deviation (dashed) and dispersion curve of minimum-misfit model (thick solid). (b, d, f): Inverted velocity models. The best 5000 models (grey), including those within 0.5 of the minimum-misfit model (sorted by decreasing misfit, red to blue), are shown; the minimum-misfit model is highlighted (yellow-black dashed line). Inset in (b) shows parametrization with major nodes 1 (surface), 2 (upper crust), 3 (lower crust) and 4 Moho. Starting models: (a, b) shallow Moho (CRUST1.0) at point 'E'; (c, d) deep Moho (Al-Hashmi *et al.* 2011) at point 'E'; (e, f) deep Moho (CRUST1.0) at point 'W'.

Downloaded from https://academic.oup.com/gji/article/231/2/817/6609440 by CNRS user on 16 March 2023

we can utilize them as independent constraints in the interpretation of the final velocity model, including to derive V_P/V_S ratios (discussed further below). The crustal V_{SV} model is expressed by four parameters describing perturbations from the isotropic background model in terms of nodes of cubic splines. The first node is located at the surface, the fourth at Moho depth. Within the crust, V_{SV} velocity perturbations from the starting model of up to 1.6 km s^{-1} are allowed during the inversion. The depth of the second and third node within the crust, as well as the Moho depth are free parameters of the inversion. The depth of the second and third node can vary by ±3 km and the Moho depth by ±5 km. The crustal V_{SH} model is described by perturbations from the V_{SV} model in terms of a cubic spline. It is also expressed by four parameters that can vary by up to ±0.5 km s^{-1}. In addition, two parameters describe the sub-Moho V_{SV} and V_{SH} velocities. A half-space is assumed below the Moho because longer periods than 40 s would be needed in the dispersion curves to resolve sub-Moho velocities. This parametrization with in total 13 parameters ensures a high variability of the considered models as well as computational efficiency. Because of the combination of the particle swarm optimization with a random local search around the considered points in the model space, the model space is widely explored and fast convergence is ensured (El-Sharkawy *et al.* 2020). The 1-D inversion of Rayleigh and Love wave dispersion curves is repeated for all 1079 1-D models in the study area, each computed with 40 000 forward calculations. The final isotropic shear wave velocity model is taken as the Voigt average of $\frac{2}{3}V_{SV} + \frac{1}{3}V_{SH}$ and radial anisotropy expressed as the difference $V_{SH} - V_{SV}$.

3 MODEL SENSITIVITIES AND UNCERTAINTIES

Although seismic surface waves are not inherently sensitive to sharp velocity contrasts such as the crust–mantle boundary, they are capable of reasonably mapping Moho depths given sufficient bandwidth of the dispersion curve and assuming a sharp contrast at the Moho (Lebedev *et al.* 2013). In the period range 10–40 s for Rayleigh waves that is most sensitive to velocity changes at typical continental Moho depths (Lebedev *et al.* 2013), the number of our data decreases (Wiesenberg *et al.* 2022) and we therefore carefully tested the vertical resolution capabilities of our inversion for Moho depth (Fig. 4). Due to larger bandwidth of Rayleigh waves across the network, this test is conducted for inversion of Rayleigh waves only with 10 000 forward models.

Previous estimates of Moho depths are available from CRUST1.0, and independent Moho depths have been reported at nine locations in northern Oman based on joint inversion of surface wave group velocities and RFs (Al-Hashmi *et al.* 2011). Both Moho depth estimates are largely consistent over the western part of the study area but reveal significant differences in the eastern part. Figs 4(a)–(d) show a comparison of inversions of the same local dispersion curve at a location in the eastern part of the study area (red diamond 'E' in Fig. 1a) for different starting models, with 20 km Moho depth based on CRUST1.0 and 42 km based on Al-Hashmi *et al.* (2011).

With a shallow initial Moho (Figs 4a and b), the local dispersion curve is well recovered by the best-fitting model and has a low final misfit value. The deep initial Moho model (Figs 4c and d) results in a much higher final misfit and is unable to replicate the data at the low and high end of the inverted frequency band. Both velocity models show rapidly increasing V_S in the top 5 km and require V_S in excess of 4 km s^{-1} at 19 km depth, either with upper mantle (shallow Moho) or very high lower crustal velocities (deep Moho). In the latter case, the contrast at the (deep) Moho becomes insignificant and interpretation of node 4 as the crust–mantle boundary would be misleading. In consequence, at this location 'E', our inversion is not able to provide a reliable estimate for Moho depth, but irrespective of that, absolute V_S must be >4 km s^{-1} at depths >20 km. The misfit of the deep-Moho scenario might be theoretically improved by adjusting the parametrization for this inversion point, for example by allowing for larger perturbations in the Moho depth. However, due to the high velocity lower crust, resolution of the Moho remains unlikely, and we prefer a simple, homogeneous parametrization for the entire study area.

While the data do not allow to infer the crust-mantle boundary in the eastern part of the study area, the example in Figs 4(e) and (f) at a location in the northwest of the study area (red diamond 'W' in Fig. 1a) demonstrates that our chosen parametrization is generally capable of recovering crustal velocity profiles with a deep Moho. Here, the dispersion curve is overall much slower than in the east (Fig. 4e) and the inversion recovers shear wave velocities below 4 km s^{-1} down to 41 km depth where it places the Moho with a clear contrast in V_S (Fig. 4f). In this case, despite uncertainties in the best-fitting models of about ±2 km, we can safely interpret a deep Moho at this location 'W'.

In summary, Moho depths can be resolved by ambient noise dispersion curves in areas where the velocity structure in the crust is not untypically fast and the crust–mantle boundary displays a clear contrast.

To account for isotropic V_S and radial anisotropy in the inversion, we jointly invert Rayleigh and Love wave dispersion curves. Fig. 5 compares inversion results at two locations in the ophiolite with two locations in the tectonic windows. Whereas the isotropic V_S models are generally well constrained, the range of possible models with low misfit is much larger for radial anisotropy. Uncertainties are particularly large in the lower crust. This is to some extent expected due to fewer Love wave phase measurements at periods >15 s and less lateral resolution in Love wave phase velocity maps (Wiesenberg *et al.* 2022). Nevertheless, despite the larger uncertainties, some important conclusions can be drawn from radial anisotropy by analysing the parameter space.

This is shown in Fig. 6 for isotropic (Figs 6b and d) and radially anisotropic (Figs 6c and e) shear wave velocity at node 2 (upper crust) at two locations in the study area. At both locations (marked in Fig. 6a), isotropic velocity perturbations are well constrained while radial anisotropy shows a broader range of possible models with low misfit. Taking the width of the point cloud at the minimum misfit plus 0.5 (red line in Figs 6b–e), we find that radial anisotropy is in the entire study area better constrained in the upper (node 2, Fig. 6f) than the lower crust (node 3, Fig. 6g). This is consistent with the examples shown in Fig. 5 where secondary maxima are not uncommon in the lower crust but less so in the upper crust. From the ensemble of best-fitting models with misfits within 0.5 of the minimum-misfit model (below red line in Figs 6b–e), we compute an 'expected model' based on the expectation value for this model parameter (red triangle in Figs 6b–e). For isotropic V_S, the expected model is generally very close to the minimum-misfit model, whereas differences between the two for radial anisotropy suggest that the sign of anisotropy may be well resolved but the absolute amplitude might be overestimated in the minimum-misfit model.

Therefore, we will restrict our interpretation of radial anisotropy to the upper crust and areas where we observe strong signals, along and north of the mountain belt, in the southern foreland as well as in the easternmost part of the study region (Fig. 6a).

Downloaded from https://academic.oup.com/gji/article/231/2/817/6609440 by CNRS user on 16 March 2023

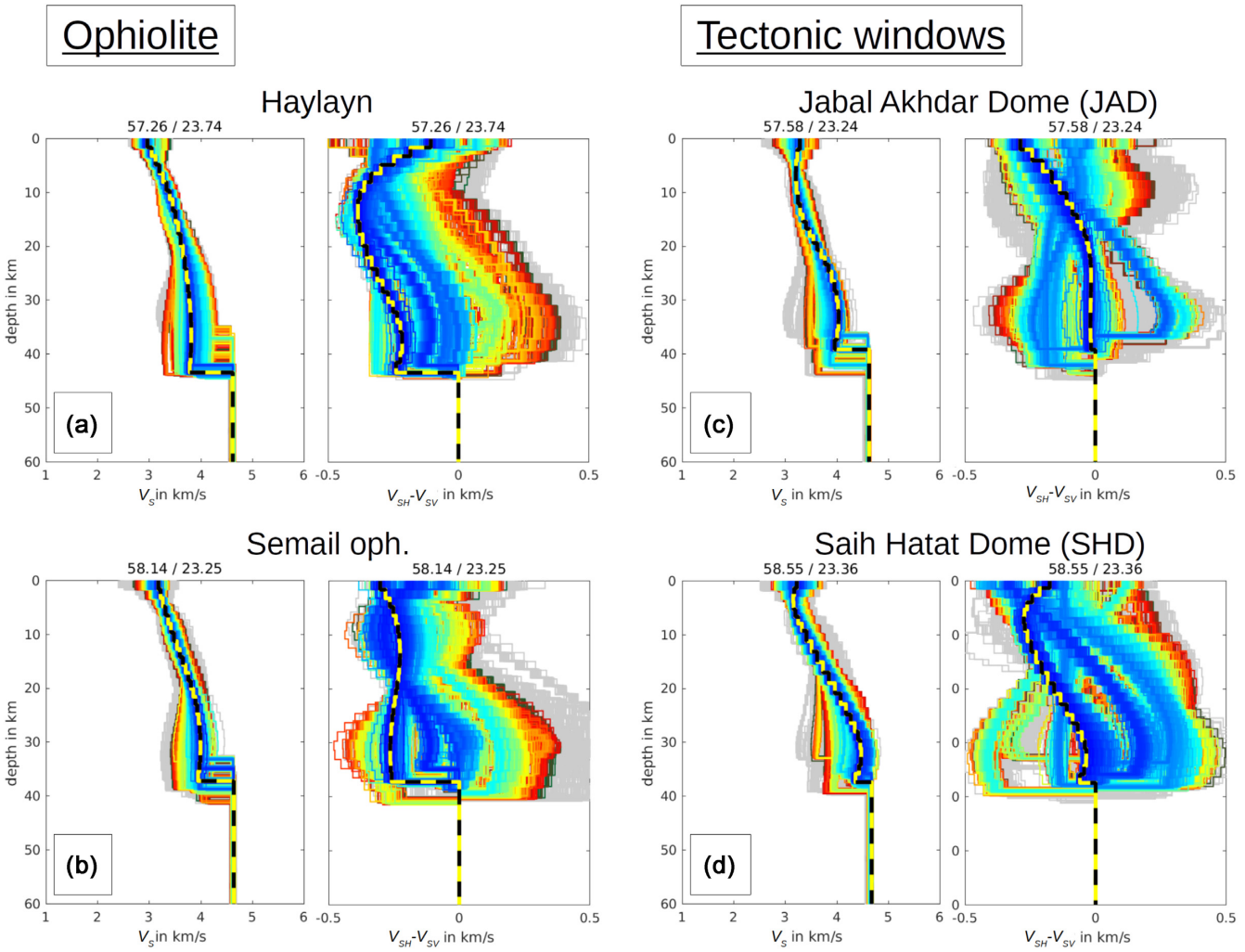

Figure 5. Inversion of local dispersion curve – Isotropic V_S and radial anisotropy. Each panel shows local 1-D model of isotropic V_S (left-hand panel) and radial anisotropy ($V_{SH}-V_{SV}$) (right-hand panel), sorted by decreasing misfit (red to blue, 5000 best-fitting models shown). Locations of points are shown as green squares in Fig. 1(a). (a) Batinah plain north of Haylayn ophiolite; (b) Semail ophiolite between JAD and SHD; (c) JAD and (d) SHD.

4 RESULTS

4.1 Geological reference profiles

Detail-rich availability of geological information as well as shallow local seismic velocity profiles from exploration geophysics (borehole, reflection seismic in the foreland, see Al-Lazki *et al.* 2002) and laboratory measurements of the ophiolite (Christensen & Smewing 1981), allows to assess the robustness of our ANT inversion results. We infer 'geological isotropic velocity models' ('geological models' in the following) at three selected locations south, within and north of the Jabal Akhdar Dome, following the profile by Al-Lazki *et al.* (2002) (Fig. 7, locations in Fig. 1a as blue hexagons).

For the geological velocity models (thin black line in Fig. 7), geological interpretation, seismic velocities of the upper crust and crustal thickness are taken from Al-Lazki *et al.* (2002) (shear wave velocity converted with $V_P/V_S = 1.73$), with slightly adjusted interface depths in the upper crust to fit geological field data (Béchennec *et al.* 1992). Seismic velocities for the middle and lower crust are averaged values from local CRUST1.0 models Laske *et al.* (2013).

In the upper crust, the geological model south of Jabal Akhdar (Fig. 7a) is covered by ∼2 km of obducted Hawasina and syntectonic Aruma sediments with low shear wave velocities (V_S) of 2.3 km s^{-1}, and underlain by distinctly faster, pre-obduction sediments of the Mesozoic Hajar Supergroup and the Pre-Permian sequence with $V_S > 3$ km s^{-1} (Al-Lazki *et al.* 2002; Aldega *et al.* 2017). North of Jabal Akhdar Dome, the ophiolite cover is expected to be ∼5 km thick and exposes high V_S of 3.2 km s^{-1} (Christensen & Smewing 1981). Inside the Jabal Akhdar Dome, V_S of the exposed pre-Cretaceous sedimentary rocks (mostly carbonates and weakly metamorphosed pre-Permian siliciclastics) is very similar (3.1 km s^{-1}) to the ophiolite to the north but much higher than the younger and less consolidated sediments in the southern foreland. The reference velocity profiles of the Jabal Akhdar and southern model are steadily increasing with depth while the northern model suggests almost constant V_S from the surface to the Precambrian basement at 13 km depth with a thin (1 km), intermittent layer of low velocity Hawasina sediments.

At each location, we select the closest inversion point of our model and show the minimum-misfit V_S model as dashed coloured line in Fig. 7. Velocity discontinuities within the crust cannot be

Downloaded from https://academic.oup.com/gji/article/231/2/817/6609440 by CNRS user on 16 March 2023

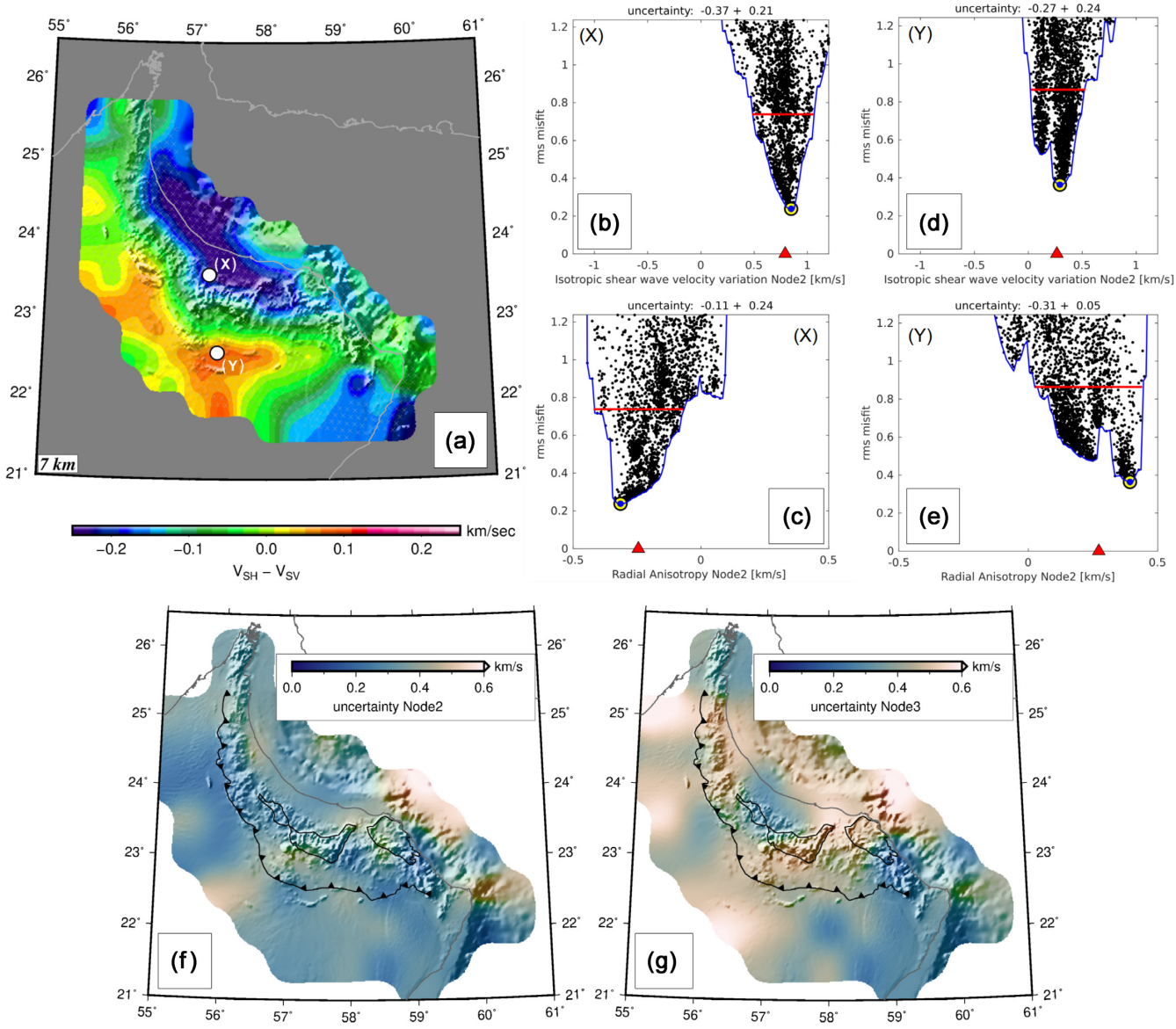

Figure 6. Uncertainties of isotropic V_S and radial anisotropy. (a) map view of radial anisotropy in the upper crust; (b–e) uncertainty of isotropic V_S (b, d) and radial anisotropy (c, e) in the upper crust at two locations [*X*, *Y*, shown in (a)]; (f, g) uncertainty at inversion node 2 (upper crust) and 3 (lower crust) as width of point clouds at min(rms_misfit)+0.5 [red lines in (b–e)].

recovered by the inversion—both due to the vertically smooth sensitivity of surface waves to variations in V_S, as well as the continuity of cubic perturbations across nodes 2 and 3 in our parametrization. Apart from that, inversion results match the geological profiles overall very well.

In the lower crust, the V_S models south and north of the Jabal Akhdar Dome show velocities >4.0 km s^{-1} below 20 and 25 km depth, respectively, while within the Jabal Akhdar Dome the lower crust is distinctly slower with velocities ∼3.8 km s^{-1}. The deviation from the geological models is more significant in this depth range because there are no a priori, local constraints on middle and lower crustal properties in the geological models beyond CRUST1.0. While both the geological and our models suggest crustal thickening beneath the Jabal Akhdar Dome, the Moho is overall 3–4 km shallower in our model than previously expected from gravity modelling and local RFs (Al-Lazki *et al.* 2002). Al-Hashmi *et al.* (2011) reported Moho depths of 38 and 40 km at locations very close to the southern and northern model, respectively, which is identical with our inversion result.

In the shallow crust, prior information in the geological models is much better constrained and our inversion replicates the expected values reasonably well. The northern model suggests a high-velocity layer above a low-velocity zone at ∼5–13 km. This is an indication that ophiolite thickness can be recovered in our model, at least if the high-velocity layer is not thinner than 2–3 km.

V_S of the ophiolite (<3.3 km s^{-1}) is very similar to that of autochthonous sedimentary rocks (3–3.3 km s^{-1}; Figs 7b, c and 5) and the discrimination between these lithologies can therefore not be easily made by V_S alone. However, there is a distinct difference in radial anisotropy between the ophiolite nappes and the tectonic windows (Fig. 6a). In the ophiolite, radial anistropy is distinctly negative, that is $V_{SV} > V_{SH}$, despite larger uncertainties than for isotropic V_S (Figs 5a and b). In the tectonic windows (Figs 5c and d), radial anisotropy is less well constrained with a tendency to

Downloaded from https://academic.oup.com/gji/article/231/2/817/6609440 by CNRS user on 16 March 2023

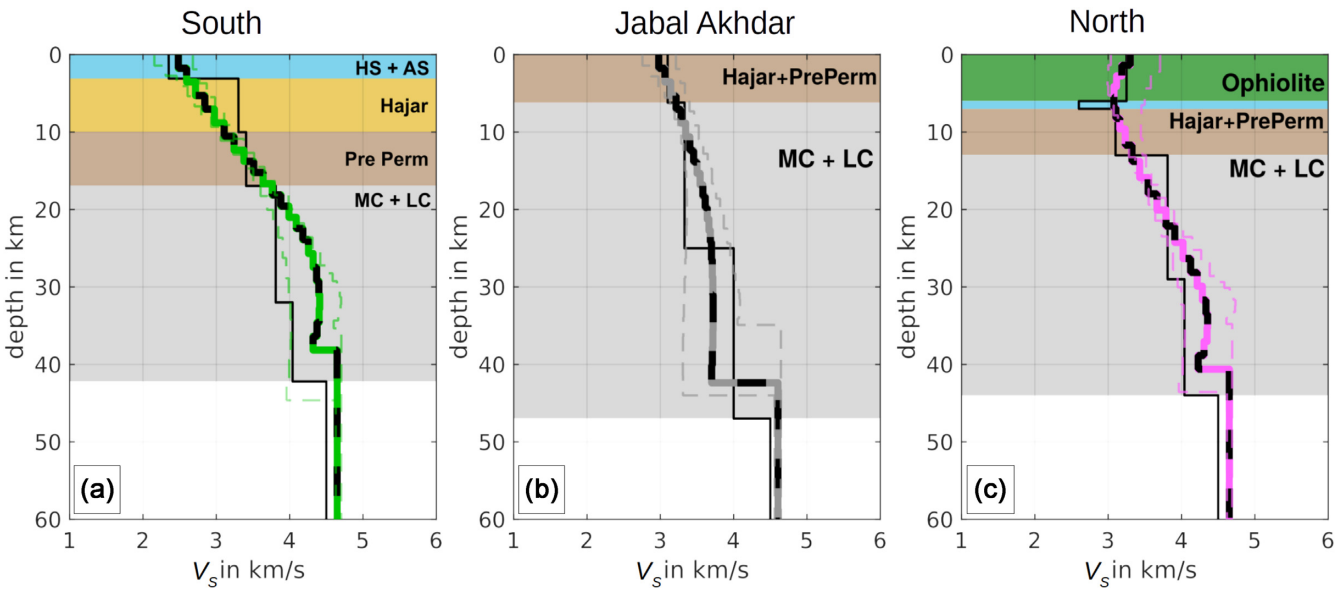

Figure 7. Comparison of local, 1-D isotropic V_S models to expected velocity profiles from a priori information (see text for details). Location of points are given in Fig. 1(a) as blue hexagons. HS + AS, Hawasina and Aruma sediments; Hajar, Permian to Late Cretaceous sediments; Pre Perm, Late Proterozoic through Palaeozoic sediments; MC, LC, middle, lower crust.

slightly negative values (Fig. 6). Since the ophiolite nappes particularly on the northern flank of the Oman Mountains are known to dip by around 30–45° to the NE (Béchennec *et al.* 1992), we interpret the distinct anisotropic signal as structural anisotropy due to a dipping medium.

4.2 3-D crustal velocity model and crustal thickness

The 3-D crustal model for northern Oman is compiled from all local 1-D inversions. We use the 'expected model' at each gridpoint, as these provide a laterally smoother and more robust 3-D model than 'minimum-misfit models' where occasionally large jumps may occur from one gridpoint to the next. The model is presented by selected horizontal slices of isotropic V_S at 2, 12, 28 and 38 km depth (Fig. 8) and 7 km depth (Fig. 9), and five vertical sections (Fig. 9). We also describe and discuss a Moho map and V_P/V_S ratios as estimated from ANT and RF in Fig. 10.

At shallow depths (Fig. 8a), the sediment-filled depression of the (offshore) Sohar Basin (Fig. 9a) to the north, and the Foredeep, Fahud and Ghaba Salt Basins (Fig. 9c) to the south of the Oman Mountains, are well outlined by distinctly low shallow V_S. Low V_S is accompanied by pronounced positive radial anisotropy (Fig. 6a) which is in line with a first-order horizontally stratified medium in the basins. The foreland is contrasted by much higher velocities across the mountainous region including the Jabal Akhdar and Saih Hatat domes. In the vertical section (Fig. 9b), shallow seismic velocities in the range 3–3.25 km s^{-1} colocate well with the ophiolite massifs and show considerable thickness variations along the profile.

Velocities are lower in the northern than central and southern massifs as seen by the deepening 3.25 km s^{-1} contour in Fig. 9(b) below the northern massifs. In the central massifs, a pronounced high-velocity anomaly has absolute velocities increasing from 3.2 km s^{-1} at 4 km to 3.7 km s^{-1} at 16 km depth. Velocities below the southern massifs are slightly lower and reach 3.5 km s^{-1} at 10 km depth. Below that, generally elevated velocities in the eastern part of the model mark the transition to a high-velocity lower crust (Fig. 9b, >400 km along the profile).

In the well-resolved Central Oman Mountains (see Wiesenberg *et al.* 2022, for details on resolution), ophiolite nappes in the southern massifs and autochthonous sedimentary rocks in the Jabal Akhdar and Saih Hatat domes are barely distinguishable in V_S alone (Figs 8a and 9f) but radial anisotropy separates the dipping ophiolite nappes from the tectonic windows (Fig. 6a). Only in the southern ophiolite massifs, where the ophiolite shows low-angle inclinations, this distinction is less pronounced. At 7 km depth (Fig. 9f), V_S of the ophiolite in the southern massif is slightly lower than inside the Saih Hatat dome where high-pressure metamorphic and mafic rocks are exposed (Figs 8a, b, 9a and b; Yamato *et al.* 2007; Chauvet *et al.* 2009; Béchennec *et al.* 1992).

East and southeast of the Saih Hatat Dome, V_S is overall close to average in the shallow crust with velocities in the range 2.8–3.2 km s^{-1} (Figs 8a, 9a and b). This is faster than V_S in the sedimentary basins south of the thrust front and, thus, suggests a shallow basement. East of the Qalhat Fault, significantly lower velocities (<2.8 km s^{-1}) are found (Figs 8a and 9a, >460 km along profile).

In the middle crust, starting at ∼12 km depth, seismic velocities are lower in the northwest and higher in the eastern part of the study area—with the exception of a high-velocity body in the central massifs (Fig. 8b). The horizontal view highlights that the transition from lower to faster velocities occurs across the NNE–SSW trending Semail Gap Fault Zone (SGFZ, Fig. 8b).

The SGFZ emerges at ∼8 km depth with a 3 per cent contrast in shear wave velocity in the north, adjacent to Saih Hatat Dome, and at ∼11 km depth it marks a lateral velocity contrast >5 per cent from the coast to the southern end of our model area. It can be traced through the middle crust to ∼16 km depth where it fades into a larger high-velocity anomaly in the lower crust (Figs 9a and c). Another distinct, NNE–SSW oriented boundary is found from ∼20 km depth downwards at the western limit of the Jabal Akhdar Dome (Figs 8c, 9a and c) and we will refer to this boundary as Western Jabal Akhdar Zone (WJAZ) in the following. The velocity contrast is ∼10 per cent at 25 km depth and ∼5 per cent at the

Downloaded from https://academic.oup.com/gji/article/231/2/817/6609440 by CNRS user on 16 March 2023

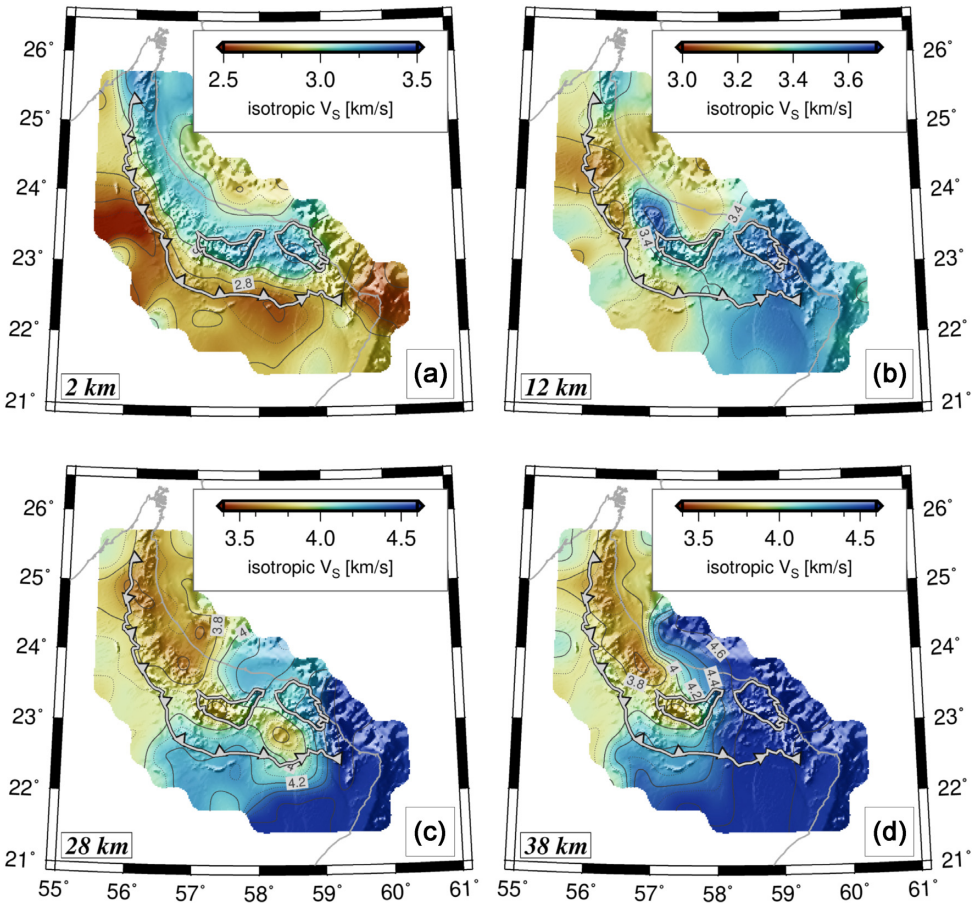

Figure 8. Map views of isotropic V_S at depths of (a) 2, (b) 12, (c) 28 and (d) 38 km.

base of the crust. Absolute velocities east and west of the WJAZ are consistently above and below 4.0 km s^{-1}, respectively.

East of the Saih Hatat Dome, another lower crustal, NNE–SSW striking boundary emerges at ∼25 km depth in the model (Figs 8c, 9a and c). Being located close to the town of Ibra, we refer to this boundary as the Ibra Zone in the following. Velocities increase across this boundary by ∼8 per cent and at 30 km depth, velocities are in excess of 4.5 km s^{-1} east of it. The domain between the Ibra and WJAZ is overprinted by velocities <4.0 km s^{-1} below the Jabal Akhdar Dome and the southern ophiolite massif in the lower crust (Figs 8c and d).

Crustal segmentation is also reflected in RFs on a profile across the network from NW to SE (Fig. 2b). Changes in general characteristics of the RF from NW to SE colocate with the three main boundaries identified above and the RF section can be subdivided in four sectors: NW of WJAZ (I), between WJAZ and SGFZ (II), between SGFZ and Ibra Zone (III) and the domain east of Ibra Zone (IV).

In sector I, early (basement) conversions group into two sets of stations, where those on the northern flank of the topography, located on top of the ophiolite show ∼zero conversion time (marked by white dot in Fig. 2b). Stations on the southwestern side of topography (without dot in Fig. 2b), on the other hand, show consistent delayed conversion arrivals of 1.4–2 s in sector I and II. We interpret them as the top of the crystalline basement at ∼10 km depth, following Zhu & Kanamori (2000, their eq. 2) and taking into account that V_S is in the range 2.5–3.25 km s^{-1} in the top 10–15 km of the velocity model in the area (see Fig 9c and d). In sector III, the shallow conversions are strongly variable across the sector. However, those in the western portion with earliest arrivals (white dot in Fig. 2b) are located between the Jabal Akhdar and Saih Hatat domes, suggesting a complex transition from west of SGFZ towards the Ibra Zone. The eastern stations within sector III show a more consistent RF pattern that converges east of the Ibra Zone in sector IV. There, sediment conversions are at 0.7–0.9 s, corresponding to 4–6 km depth, which is consistent with a thinner sedimentary cover and a shallow crystalline basement in this area (e.g. Wyns *et al.* 1992).

This overall behaviour is reflected in sector-wise RF stacks (Fig. 2b, right-hand panel) which also highlights distinct variations in the Moho conversion times at 3–5 s. Moho conversion in sector II is slightly later than in sector I. However, the difference in mid-to-lower crustal V_S across the WJAZ (Figs 8c,d, 9a and c) prohibits the direct inference of a deeper Moho. The broad Moho signal in the stack of sector III reflects a complex structural transition between the SGFZ and the Ibra Zone while in sector IV, early Moho arrivals suggest a shallowing of the Moho.

We convert RF delay times of Moho arrivals (Fig. 2b) to depth using the IASP91 model with a V_P/V_S ratio of 1.73 in the crust to derive a map of Moho depths from RF (RF-Moho in the following, Fig. 10a). We deliberately do not use crustal average V_S velocities from the model but prefer an independent estimate of Moho depth from RF. This is because (i) we need to assume a V_P/V_S ratio to migrate RF conversion times to depth and (ii) the model resolution in the east does not allow us to infer a Moho depth from the ANT inversion which makes computation of a crustal average V_S to some extent arbitrary. The benefit of keeping the datasets separate at this

Downloaded from https://academic.oup.com/gji/article/231/2/817/6609440 by CNRS user on 16 March 2023

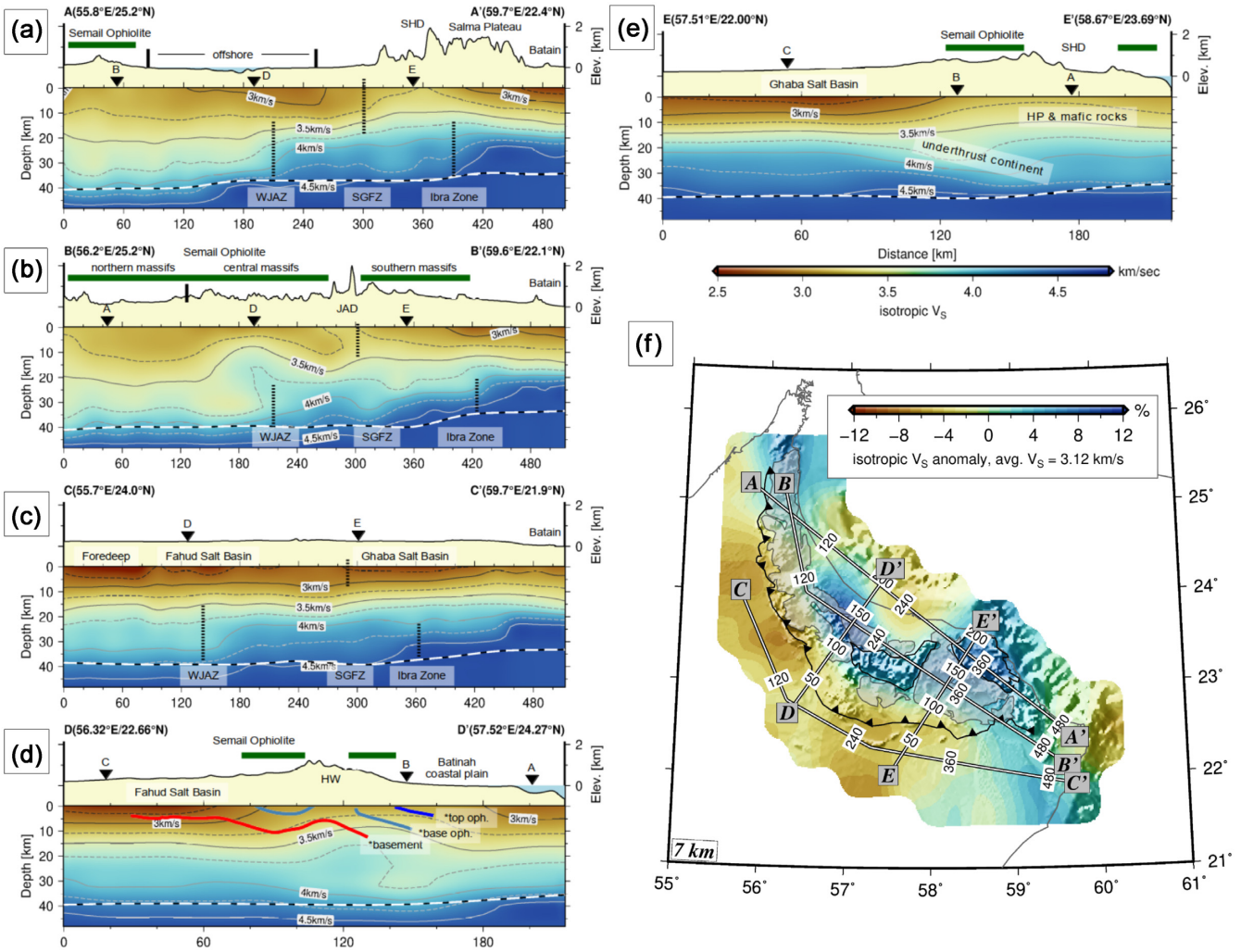

Figure 9. Vertical sections through isotropic V_S model. Profile locations are shown in map view at 7 km depth (f). Coloured, asterisk annotated contours in (d) are from Searle (2007), ∗basement is top Pre-Permian. Abbreviations: HW, Hawasina Window; JAD, Jabal Akhdar Dome; SGFZ, Semail Gap Fault Zone; SHD, Saih Hatat Dome; WJAZ, Western Jabal Akhdar Zone.

stage is that an independent estimate of Moho depth from RF allows us later to infer V_P/V_S ratios by combining the results from the two methods (see Section 5).

In the northwest, Moho depths are 35–45 km with the largest values below and slightly northeast of the topography. Moho depths less than 36 km are suggested in the Foredeep west of the allochthonous thrust front but the ANT velocity model suggests a deeper Moho at 38–40 km depth (Fig. 9c). In the Central Mountains, RF-Moho is deepest south of the mountain belt, again in contradiction to observations from the ANT model (Fig. 7). In both cases, a laterally varying V_P/V_S ratio could converge these two independent observations and we will discuss this further below. East of the Ibra Zone, where ANT Moho depths cannot be reliably resolved due to the high velocity lower crust, the depth of RF-Moho decreases to 35 km and further to 30 km on the eastern coast.

We apply the ZK stacking method (Zhu & Kanamori 2000) to assess tradeoffs between Moho depth and V_P/V_S ratio across the study area. As crustal multiples are in many cases not easy to identify in the unfiltered RF traces of our data set, the method was only applicable to selected stations where stack results with reasonable quality were obtained for low-pass filtered traces (see Figs 11a and b for examples). For all obtained results, the resolution regarding discontinuity depth is, due to the low frequencies, of the order of ±5 km. For the V_P/V_S ratios, resolution is less and only a tendency of lower or higher values can be inferred for each station. Over the entire study area, computed from a subset of 8–32 s low-pass filtered RF and well constrained stacks, V_P/V_S ratios cluster at 1.85 ±0.12 for P-RF (average for 29 stack results) and 1.81 ±0.12 for S-RF (average for 19 stack results). The regionally averaged Moho depth values obtained for P-RFs, bandpass filtered at 8–32 s (Fig. 11c), do not differ much from those derived from picking of the arrival time of the Ps Moho converted phase (Fig. 10a) but there is an overall tendency towards slightly increased Moho depths from ZK-stacking. S-RF-ZK-stacks results do overall not differ but are in most cases less well constrained (not shown). For the RFs filtered at 4–30 s, the maximum semblance is found at mid-crustal level for many stations in the south and southeast but also to the north of the network (Figs 11b and d). Distinct exceptions are found near the northeastern coast around the Saih Hatat Dome where a group of four stations shows very deep discontinuity depths in the range 54–58 km. However, all these stations (inset in Fig. 11d) show an equally pronounced maximum in the semblance map at ∼30–35 km depth, which is in line with our Moho depth inferred from RF and ANT for the area.

Downloaded from https://academic.oup.com/gji/article/231/2/817/6609440 by CNRS user on 16 March 2023

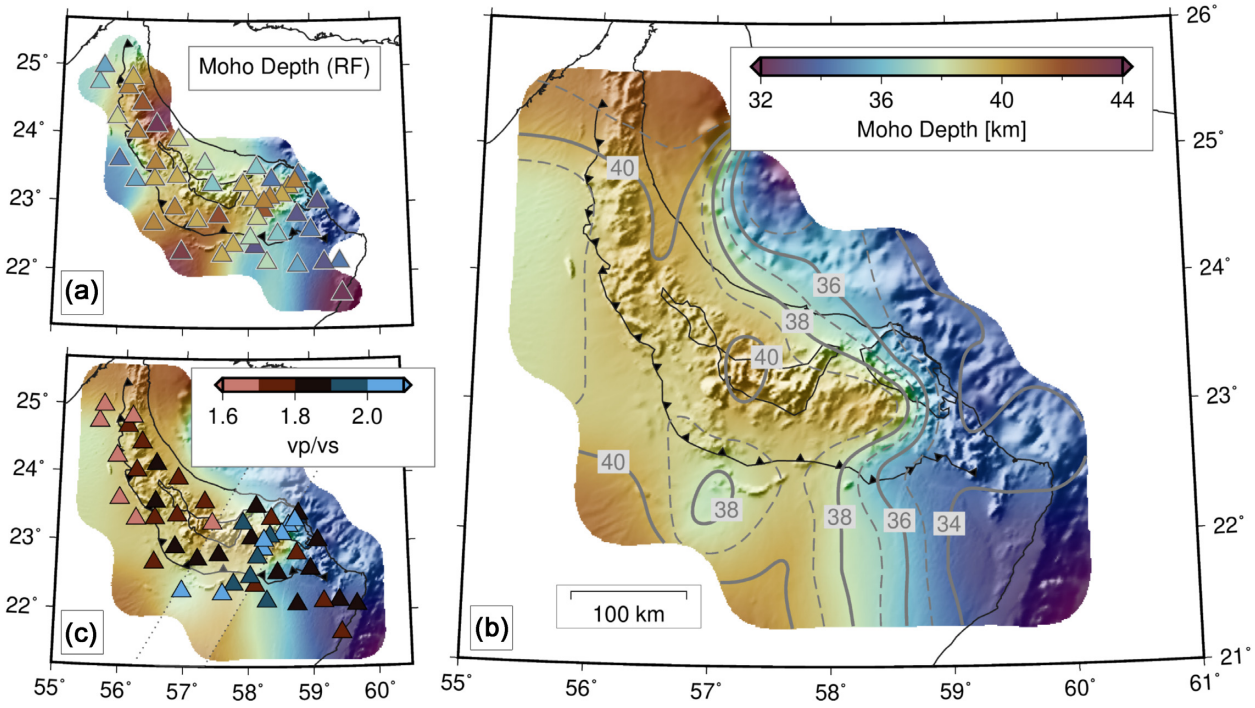

Figure 10. Moho map from RF, combined Moho map and crust-average V_P/V_S ratio. (a) Moho map interpolated from localized RF estimates. (b) combined Moho map from ANT (NW) and RF (east). (c) Same as (b) with station-wise V_P/V_S ratios computed by fitting RF delay times to crustal V_S model. The opaque area in the central part is a 'transition zone' between the ANT and RF Moho (see text for details).

5 DISCUSSION

In the tomographic model, the depth of node 4 (Moho node, ANT-Moho in the following) is in the northwestern part of the study area a reliable estimate where mantle velocities >4.4 km s^{-1} are reached (section 3, Figs 4 and 7). NW of WJAZ, ANT-Moho depths are ∼38–40 km in the foreland and increase from 40 to 44 km northeastwards of the thrust front, in line with previous interpretations (Ravaut *et al.* 1997; Ali *et al.* 2020). Moreover, ANT and RF Moho estimates differ by no more than 3 km in this area and are comparable to CRUST1.0.

East of the SGFZ, however, Moho depth is not resolved in ANT (Section 3). The Moho sensitivity test (Fig. 4) has shown that high seismic velocities in excess of 4.0 km s^{-1} are required below ∼20 km depth—irrespective of the depth to Moho in the starting model. The depth of node 4 in ANT is therefore not the Moho but is related to the top of a very high velocity lower crust that we can identify in ambiguous signals in the ZK stacks of RF (Figs 11b and d).

Given the fit of RF- and ANT-Moho in the northwest and the unavailability of ANT Moho in the east, we construct a combined Moho map from ANT-Moho in NW and RF-Moho in SE (Fig. 10b, Moho depths at station locations are listed in Tab. A1). In the 'transition zone' between JAD and the Ibra Zone (dotted lines in Fig. 10c), Moho depths are interpolated by continuous curvature spline interpolation (Wessel *et al.* 2019) which preserves the principal aspects of Moho depth in the vicinity of JAD and SHD.

The comparison with expected velocity models based on prior information (Fig. 7) showed that ANT Moho depths along a profile across the Jabal Akhdar Dome are likely shallower than earlier proposed (Al-Lazki *et al.* 2002), confirming Al-Hashmi *et al.* (2011) who reported Moho depths of 38 and 40 km at locations south and north of the dome. Al-Lazki *et al.* (2002) obtained Moho depths from RF analysis of 9 teleseismic events with magnitudes <6 whereas Al-Hashmi *et al.* (2011) and this study used >50 events with magnitudes >5.5. Moreover, the profile by Al-Lazki *et al.* (2002) was modelled with relatively low densities of 2.7 g cm^{-3} throughout the entire middle and lower crust to fit the gravity data to their RF observations. In light of the lateral variability in V_S and the high velocities south and north of Jabal Akhdar Dome, higher densities in the middle and lower crust would give room for fitting the gravity data also to a shallower Moho. Below the Jabal Akhdar Dome, velocities are <3.8 km s^{-1} down to 35 km depth and ANT shows a clear discontinuity to mantle velocities at 42 km depth (Fig. 7).

RF-Moho depths across Jabal Akhdar Dome from south to north suggest a very deep Moho of 46 km south of the thrust front and a drastic Moho shallowing to <36 km north of the Jabal Akhdar Dome (Fig. 10a). This south-to-north trend is contrary to previous observations and likely contains a bias from the heterogeneous velocity structure. S-RF suggest later conversion times south and north of the dome whereas P-RF are missing north of JAD due to insufficient data quality at the coastal stations (Fig. 3). Therefore, a minor deepening of the Moho below the Jabal Akhdar Dome is overall more consistent than a south-to-north trend.

Moho depths derived from a modified ZK stacking method (Fig. 11c) tend to be up to 5 km deeper than those found from picking the Ps (Moho) arrival (Fig. 10a). The effect is more pronounced in S-RF results than in P-RF results and is stronger in the RFs filtered from 8 to 32 s than in the RFs filtered from 4 to 30 s, but the depth difference is often in the range of the uncertainty of the stack peak width. A difference may be expected because the local ANT V_S model differs from the crustal velocities of the IASP91 model used for migrating delay times of the converted phases (from Figs 3a to 10a). The observation may also indicate that the Moho is not a sharp discontinuity but is more likely a gradient zone with a width of several kilometres. In contrast, the mid-crustal discontinuity observed in the south and southeast of the network is better

Downloaded from https://academic.oup.com/gji/article/231/2/817/6609440 by CNRS user on 16 March 2023

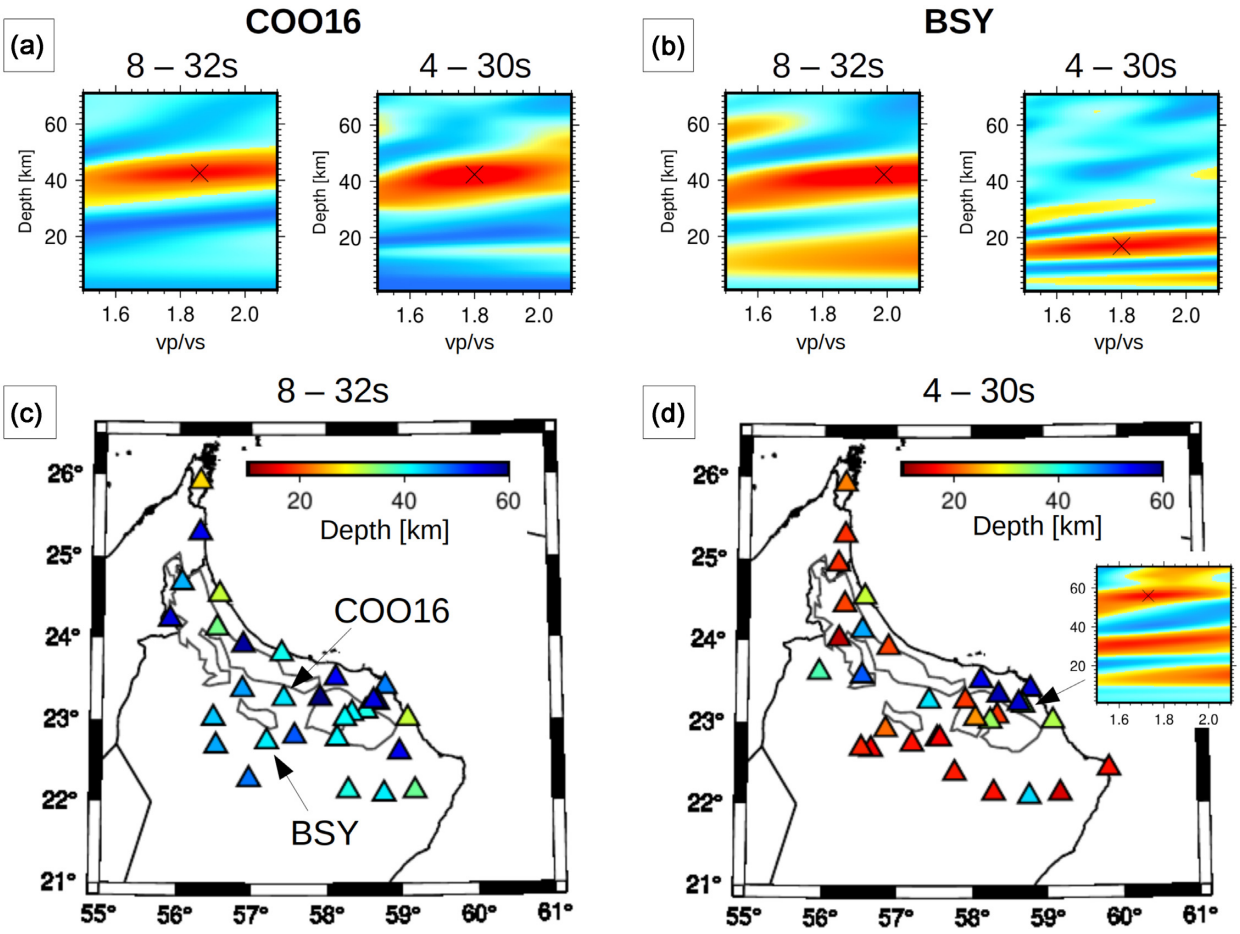

Figure 11. ZK Analysis after Zhu & Kanamori (2000). (a, b) Depth-V_P/V_S ratio semblance maps for two stations (shown in c) computed from RF filtered with bandpasses 8–32 s and 4–30 s period. Red/blue is high/low semblance, respectively. (c, d) Depth to maximum semblance for each analysed station in period range 8–32 s (c) and 4–30 s period (d). Inset in (d) shows depth-V_P/V_S map for a station in Saih Hatat Dome.

observable in the data filtered from 4 to 30 s and this likely indicates a regionally sharper transition between upper and lower crust. Four stations around the Saih Hatat Dome show a deep discontinuity at 54–58 km depth (bandpass filtered 4–30 s, see Fig. 11d) but the stacks similarly indicate the presence of a discontinuity at the depth level of the Moho from RF and ANT (30–35 km).

In the Saih Hatat Dome, a Moho at ∼35 km depth is in line with both observations from RF and ANT and is well preserved in the combined Moho map (Fig. 10b). Both P- and S-RF show larger delay times south of the Saih Hatat Dome which suggests that the mildly thickened crust below the Jabal Akhdar Dome extends eastwards below the southern ophiolite massifs.

RF are widely used to infer not only Moho depths but also V_P/V_S ratios using the method by Zhu & Kanamori (2000). However, the data does not allow to make reasonable inferences on lateral variability of crust-average V_P/V_S ratios using this approach (Fig. 11). Instead, we use the combined Moho map to compute station-wise V_P/V_S ratios by fitting RF delay times to the 3-D shear wave velocity model (Fig. 10c, V_P/V_S ratios at station locations are listed in Table A1). North of the allochthonous thrust front, within the Central and Northern Oman Mountains, V_P/V_S ratios are 1.7–1.8, very typical for bulk continental crust and in line with previous estimates (Al-Hashmi *et al.* 2011). A large variety of typical crustal rock compositions cover this V_P/V_S range (Christensen 1996), not only of the crystalline crust but also of the ophiolite where V_P/V_S ratios of ∼1.8 have been measured from rock samples (Christensen & Smewing 1981). South of the thrust front, in the foredeep, earlier P-to-S delay times in RF convert to smaller V_P/V_S ratios of 1.6–1.7. While the lower crust here is similar to that north of the thrust front in terms of V_S, the upper crust is significantly slower (Fig. 9f). Low and decreasing V_P/V_S ratios are associated with a SiO_2 increase of SiO_2-rich rocks (>55 per cent wt per cent, Christensen 1996) and sandstone, the dominant Palaeozoic lithology in northern Oman (Loosveld *et al.* 1996) has particularly low $V_P/V_S < 1.6$ at upper crustal pressures (Ji *et al.* 2018).

In the 'transition zone' between the WJAZ and the Ibra Zone, the inferred V_P/V_S ratios are very high and likely ill-constrained. With the exception of the Jabal Akhdar Dome, absolute V_S is >4.0 km s^{-1} east of the WJAZ below 25 km depth and the sharp increase in lower crustal V_S makes a general compositional change to a more mafic lithology across the WJAZ the most likely explanation. Although the ophiolite cover in the southern massifs is less than 20 per cent of the entire crust, it likely also contributes to the high crust-average V_P/V_S ratio. Manghnani & Coleman (1981) postulated extensive serpentinization of the peridotite in the southern massif that our model supports by slightly lower V_S than in the other ophiolite massifs (Fig. 9b). Moreover, serpentinization would further enhance V_P/V_S ratios (Christensen 2004), which is in line with our observations.

East of the Ibra Zone, V_P/V_S ratios are on average 1.82. This is rather high but could be explained by a strongly mafic middle

Downloaded from https://academic.oup.com/gji/article/231/2/817/6609440 by CNRS user on 16 March 2023

and lower crust that constitutes 50–80 per cent of the crustal stack. Although V_P/V_S ratios are subject to larger uncertainties in this area due to the very high lower crustal V_S (Fig. 10c), V_P/V_S ratios <1.8 are incompatible with our data. Such values would require Moho depths larger than ∼38 km in northeastern Oman, for which we have no evidence. Therefore, the most likely explanation for the high-density lower crust is a strongly mafic composition.

5.1 Tectonic interpretation

During the assembly of the African-Arabian plate in Neoproterozoic times, NE/SW-elongated terranes were accreted to the plate (Allen 2007). In light of the distinct contrast in V_S in the lower crust, as well as a change in V_P/V_S ratios, we interpret the domain east of the WJAZ as an accreted terrane, enriched in mafics. East of the Ibra Zone, very high mid and lower crustal V_S >4.0 km s^{-1} and V_P/V_S ratios of 1.82, on average, suggest a strongly mafic composition, potentially intruded by large underplated mafic to ultramafic sills or even (possibly serpentinized) mantle. In strong contrast, the physical properties of the Arabian crust west of the WJAZ suggest a typical continental, felsic composition (Rodgers *et al.* 1999) with $V_S <$ 3.8 km s^{-1} and average V_P/V_S ratios of 1.72.

Our combined Moho map is to first order consistent with the global model CRUST1.0 (Laske *et al.* 2013) and gravity-derived Moho maps (Jiménez-Munt *et al.* 2012; Mechie *et al.* 2013) who display a thinning crust from NW to SE across northeastern Arabia. However, our model establishes in detail a relatively sharp lateral transition from the thick Arabian crust (∼40 km) in northwestern Oman to thicknesses of 30–35 km in northeastern Oman which is larger than proposed by CRUST1.0. The transition from thicker to thinner crust occurs between the Semail Gap Fault and the Ibra Zone over <100 km horizontal distance and is accompanied by increasing lower crustal V_S between the WJAZ and Ibra Zone (Fig. 9c). These boundaries are straight, NNE-oriented features in the lower crust of the model whereas the SGFZ is a similarly linear structural boundary only in the upper ∼16 km of the crust. We therefore interpret these structures as being established during plate assembly in Late Proterozoic and they likely acted as predefined zones of weakness in subsequent tectonic episodes.

Whether the Ibra Zone is another terrane boundary or a crustal-scale fault remains inconclusive. Although it is neither traceable in the upper crust, nor a geological feature at the surface, it colocates with a distinct change in surface geology.

From north to south, it separates the SHD from the presently uplifting Salma Plateau (Moraetis *et al.* 2018), marks the eastern limit of significant ophiolite exposures and bounds the Ghaba Salt Basin eastward to a shallow basement that extends the Huqf High in SE Oman to the NE (Rickards *et al.* 2010). In the lower crust, the Ibra Zone is a distinct boundary with very high V_S east of it. Westwards, these very high velocities gradually fade until the SGFZ, which we interpret as the western bound of most of the mafic intrusions. This partly explains the difference in upper crustal properties between the Saih Hatat and Jabal Akhdar Dome. Modification of the lower crust most likely occurred during breakup of Pangea in Permian times on both the eastern and northern margins of present-day Oman. Northeastern Oman was located at a triple-junction at the time and breakup is associated with massive magmatism, evidenced by abundant Permian mafic rocks in the SHD (e.g. Chauvet *et al.* 2009). Beside the intrusions into the crust, it is conceivable that originally thinned crust (by continental extension) was thickened by underplating east of the Ibra Zone.

Besides the difference in abundance of Permian mafic rocks between the Saih Hatat and Jabal Akhdar Dome, a shallower Moho below the former is in line with geodynamic interpretations of differential stretching during Pangea breakup and differential exhumation of the two domes in the late obduction stage (Ninkabou *et al.* 2021). Moreover, the difference in upper crustal V_S between the two domes, with faster velocities in SHD than JAD (Fig. 8b) is consistent with a difference in metamorphic degree of continental rocks exhumed after obduction. Rocks in the Saih Hatat Dome expose High Pressure—Low Temperature metamorphism of up to eclogite-facies conditions (∼80 km depth), whereas the Jabal Akhdar area shows only mild metamorphism and was, thus, dragged only marginally into the subduction zone (e.g. Searle *et al.* 2004; Warren *et al.* 2005; Hansman *et al.* 2017, 2021).

The WJAZ is a hitherto undescribed feature in the tectonics of northern Oman. Similar to the Ibra Zone, it has no distinct surface expression but it separates the Jabal Akhdar Dome from the Hawasina Window. On the northern flank of the Hawasina Window, a pronounced high V_S feature that is bounded to the east by the WJAZ colocates with the Haylayn Ophiolite Massif, the presumably thickest ophiolite nappe in northern Oman (Fig. 1a, Ravaut *et al.* 1997).

Interpretation of absolute V_S to infer ophiolite thickness is subject to a number of challenges: (i) surface waves are less sensitive to velocity contrasts at depth than to (integrated) absolute V_S over a certain depth range; (ii) we can not expect a good vertical resolution within the top 5 km of our model due to decreasing number of phase-velocity measurements at periods below 10 s period and (iii) Mesozoic and older sediments have shear wave velocities similar to oceanic crustal and serpentinized mantle rocks (Fig. 8a, see discussion above). In the RF stacks (Fig. 2b), we do not observe a negative signal that could be associated with a negative velocity discontinuity at the base of the ophiolite to the (slower) top continent. This can be understood such that the base ophiolite 'fades' into the continental basement in terms of V_S. An early positive RF-conversion at 0.7–2 s can, at many locations, be associated with the base sediment conversion (Fig. 2b, sector stacks I, II, IV). The very early conversions close to zero delay time observed at locations in the ophiolite (dotted traces in Fig. 2b, locations in Fig. 1b) are most likely an artefact of imperfect rotation into the true LQT system during RF processing where we used theoretical incidence angles from the global reference model IASP91 (Kennett & Engdahl 1991).

Radial anisotropy is a good indicator to separate dipping ophiolite units from other high-V_S regions (Figs 6, 5). Within the Jabal Akhdar and Saih Hatat domes, radial anisotropy is distinctly lower in amplitude than across the ophiolite massifs along the north flank of the Northern and Central Oman Mountains and we interpret radial anisotropy in the obducted units primarily because of structural heterogeneity of the northward dipping obducted units. Inclinations of the Semail Ophiolite's Moho have been mapped to dip moderately to the northeast (Nicolas *et al.* 1996), which is supported by interpretations that the ophiolite nappes extend northeast offshore below the Sea of Oman (Manghnani & Coleman 1981; Ravaut *et al.* 1997; Al-Lazki *et al.* 2002; Ali *et al.* 2020; Ninkabou *et al.* 2021). In the southern massif, a syncline setting of the allochthonous units (Manghnani & Coleman 1981) is compatible with a reduced radially anisotropic signal.

In the Northern Mountains, we infer an ophiolite thickness of ≤10 km (Figs 9b and f), that possibly thickens further northwards (Figs 8b and 9f, Ali *et al.* 2020). The ophiolite thins southeastwards and is <5 km in the Hilti-Fizh nappes (Fig. 9f, Nicolas *et al.* 2000). A distinct change in ophiolite thickness is associated with

Downloaded from https://academic.oup.com/gji/article/231/2/817/6609440 by CNRS user on 16 March 2023

the transition from the northern to the central massifs where the Haylayn Ophiolite Massif marks the deepest reaching ophiolite, possibly down to ∼16 km depth (Fig. 9b) based on the depth where the anomaly from Fig. 8(b) 'disappears'. Although this cannot be confirmed in terms of seismic velocity, a depth of base ophiolite of up to ∼15 km below the Batinah Coastal Plain is in line with gravity models (Ravaut *et al.* 1997) and conforms to geological interpretations of the depth structure across the Hawasina Window (Fig. 9d, Searle 2007). The overlay of the deep-structure interpretation by Searle (2007) on our shear wave velocity section in Fig. 9(d) colocates the shallowing of Pre-Permian basement below the window, as well as NE-dipping V_S-iso-contours with ∼20° with the geologically inferred dip angle of the autochthonous and allochthonous units. To distinguish the base ophiolite from the underlying continental basement requires further attention, for example by revised gravity modelling that takes into account the crustal heterogeneity in V_S.

The high-velocity anomaly associated with the Haylayn Ophiolite Massif overlaps in area with the Batinah Mélange north of the Hawasina Window. The Batinah Mélange consist of slivers of Hawasina rocks, metamorphic sole and ophiolite rocks on top of the Semail Ophiolite. This inverted tectonostratigraphy has been explained as either a separate thrust sheet, unrelated to the Hawasina nappes (Carney & Welland 1974) or it might have formed during possible diapiric rise of mélange material within a fault zone during thrusting (Woodcock & Robertson 1982). Low-level thermal maturity of Hawasina rocks in the Batinah Mélange suggests gravity-driven transport over the ophiolite which had thickened by shortening during obduction (Aldega *et al.* 2021). Alternatively, the allochthonous nappes (Hawasina and ophiolite) may have thrusted over each other and doubled their thickness during obduction. This can explain the enormous thickness (16 km) of the high-velocity anomaly. During doubling of the allochthonous nappes, some shales, rocks of the metamorphic sole and ophiolite were brought towards the top of the upper allochthonous nappe and distributed via gravity flow similar as discussed in Aldega *et al*. (2021).

The velocity structure in the lower crust below the northern flank of the Hawasina Window (3.75 km s^{-1} contour in Figs 9b and d) suggests a complicated deformation that might involve thickened pre-obduction shelf units, similar as below the Jabal Akhdar Dome. South of the Hawasina Window, Pre-Permian sediments with intermittent Precambrian/Cambrian salt of considerable thickness maintain low seismic velocities in our model down to the Precambrian basement at >10 km depth, similar to south of the Jabal Akhdar Dome (Droste 1997; Al-Lazki *et al.* 2002). The ophiolite north of the Jabal Akhdar Dome is ∼5 km thick (Fig. 7c, Al-Lazki *et al.* 2002), whereas the southern massifs (east of Jabal Akhdar Dome) are ∼10 km thick (in line with Manghnani & Coleman (1981) and Ravaut *et al.* (1997)). The slightly lower shear wave velocities in the southern, as compared to the other massifs, might relate to a higher degree of serpentinization as proposed by Manghnani & Coleman (1981).

In summary, our observations are broadly consistent with gravity modelling (Manghnani & Coleman 1981; Ravaut *et al.* 1997; Al-Lazki *et al.* 2002) but provide important new insight into lateral heterogeneity of the middle and lower crust. Our 3-D model shows that the properties of the easternmost Arabian continental crust change from 'typically continental' to a (likely more mafic) lithology with mafic intrusions and/or underplated lower crust. Thus, the model provides a sound basis for reevaluating the gravity field taking into account segmentation and structural variability of the crust below the Semail Ophiolite. Furthermore, it allows for a reappraisal of the tectonic evolution of the eastern Arabian lithosphere and the relation of inherited structures on the geometry and dynamics of obduction that is subject to a separate study.

6 CONCLUSIONS

Ambient noise seismic tomography and receiver function analysis from a temporary seismological dataset acquired in northern Oman provide for the first time insight into the seismic properties of the middle and lower crust, as well as a consistent Moho map below the iconic Semail Ophiolite.

The 3-D radially anisotropic shear wave velocity model highlights a NNE-striking, hitherto unknown deep crustal boundary, located at the western margin of the Jabal Akhdar Dome (termed the Western Jabal Akhdar Zone, WJAZ) that divides the Arabian crust in two domains. West of the WJAZ, Moho depths are 40–44 km and seismic properties are typical for felsic continental crust. East of the WJAZ, lower crustal V_S is consistently above 4.0 km s^{-1} and crust-average V_P/V_S ratios suggest a compositionally different, likely mafic, lithology. East of the Semail Gap Fault, lower crustal V_S gradually increases further to 4.2–4.4 km s^{-1}. East of the Ibra Zone, another deep crustal boundary, crustal thickness decreases to 30–35 km and very high lower crustal V_S is interpreted as mafic intrusions into, and possible underplating of the Arabian continental crust during Permian breakup of Pangea.

Topography of the Oman Mountains is supported by a mild crustal root and Moho depths below the highest topography, the Jabal Akhdar Dome, are ∼42 km and, hence, thinner than previously reported. In the shallow crust, our model gives a consistent overview of lateral variability in ophiolite thickness. The thickest section (≲16 km) is found north of the Hawasina Window and bound to the east by the WJAZ. Radial anisotropy is robustly recovered for the upper crust across the study area and aids in discriminating dipping ophiolite nappes from autochthonous sedimentary rocks and shallow basement that are indistinguishable in isotropic V_S alone. Our image of lateral variations in physical properties of the northern Oman crust offers a wide range of opportunities to reappraise, for example legacy gravity models or the geodynamic evolution of the eastern Arabian margin.

ACKNOWLEDGMENTS

We are grateful to Céline Ducassou and the German University of Technology (GUtech), Oman, Dr Issa El-Hussain, Earthquake Monitoring Center (EMC) at Sultan Qaboos University (SQU), Oman, and Cécile Prigent (UJF Grenoble, now at IPG Paris, France) for their enormous support of the seismic experiment. Numerous GUtech and SQU students are thanked for their participation in the field. Seismic equipment for the temporary deployment was provided by the German Geophysical Instrument Pool (GIPP) at GeoForschungsZentrum Potsdam. The acquired waveform data set is complemented by waveform data from the Oman Seismic Network provided by the EMC. We thank Kamal Atiya from the Dubai Seismic Network for facilitating data usage, and acknowledge use of data from IRIS/IDA Global Seismic Network station II.UOSS (Scripps Institution Of Oceanography 1986). We thank Walter D. Mooney and an anonymous reviewer for thorough and constructive reviews. Figures were produced with Generic Mapping Tools (Wessel *et al.* 2019) making use of colour maps from Crameri *et al.* (2020), Matlab and Python. LW and AE were supported by DFG grant WE 4069/6-1.

Downloaded from https://academic.oup.com/gji/article/231/2/817/6609440 by CNRS user on 16 March 2023

DATA AVAILABILITY

Seismic waveform data from the temporary experiment (https://doi.org/10.7914/SN/5H_2013) can be obtained from the GEOFON data centre of the GFZ German Research Centre for Geosciences (https://geofon.gfz-potsdam.de/). Data from Oman and Dubai Seismic Network stations in the project period can be obtained from the authors upon request. Data from Global Seismic Network Stations used in this study (https://doi.org/10.7914/SN/II) are distributed by IRIS Data Management Center (https://ds.iris.edu/).

REFERENCES

Agard, P., Jolivet, L., Vrielynck, B., Burov, E. & Monié, P., 2007. Plate acceleration: the obduction trigger?, *Earth planet. Sci. Lett.,* **258**(3–4), 428–441.

Agard, P., Searle, M.P., Alsop, G.I. & Dubacq, B., 2010. Crustal stacking and expulsion tectonics during continental subduction: P-T deformation constraints from Oman, *Tectonics,* **29**(5), doi:10.1029/2010TC002669.

Al-Hashmi, S., Gök, R., Al-Toubi, K., Al-Shijbi, Y., El-Hussain, I. & Rodgers, A.J., 2011. Seismic velocity structure at the southeastern margin of the Arabian Peninsula, *Geophys. J. Int.,* **186**(2), 782–792.

Al-Lazki, A., Seber, D., Sandvol, E. & Barazangi, M., 2002. A crustal transect across the Oman Mountains on the eastern margin of Arabia, *GeoArabia,* **7**(1), 47–78.

Aldega, L., Carminati, E., Scharf, A. & Mattern, F., 2021. Thermal maturity of the Hawasina units and origin of the Batinah Mélange (Oman Mountains): insights from clay minerals, *Mar. Petrol. Geol.,* **133,** doi:10.1016/j.marpetgeo.2021.105316.

Aldega, L., Carminati, E., Scharf, A., Mattern, F. & Al-Wardi, M., 2017. Estimating original thickness and extent of the Semail Ophiolite in the eastern Oman Mountains by paleothermal indicators, *Mar. Petrol. Geol.,* **84,** 18–33.

Ali, M.Y., Watts, A.B., Searle, M.P., Keats, B., Pilia, S. & Ambrose, T., 2020. Geophysical imaging of ophiolite structure in the United Arab Emirates, *Nat. Commun.,* **11**(1), doi:10.1038/s41467-020-16521-0.

Allen, P.A., 2007. The Huqf Supergroup of Oman: basin development and context for Neoproterozoic glaciation, *Earth-Sci. Rev.,* **84,** 139–185.

Béchennec, F., Roger, J., Le Métour, J. & Wyns, R., 1992. Geological map of Seeb, sheet NF 40-03, scale 1:250,000, with explanatory notes, Tech. rep., Directorate General of Minerals, Oman Ministry of Petroleum and Minerals.

Bensen, G.D., Ritzwoller, M.H., Barmin, M.P., Levshin, A.L., Lin, F., Moschetti, M.P., Shapiro, N.M. & Yang, Y., 2007. Processing seismic ambient noise data to obtain reliable broad-band surface wave dispersion measurements, *Geophys. J. Int.,* **169**(3), 1239–1260.

Berkhout, A.J., 1977. Least-squares inverse filtering and wavelet deconvolution, *Geophysics,* **42**(7), 1369–1383.

Blendinger, W., van Vliet, A. & Clarke, M. W.H., 1990. Updoming, rifting and continental margin development during the Late Palaeozoic in northern Oman, *Geol. Soc., Lond., Spec. Publ.,* **49**(1), 27–37.

Carney, J.N. & Welland, M. J.P., 1974. Geology and mineral resources of the Oman Mountains, A reconnaissance survey of parts of the Sultanate of Oman. IGS, Overseas Div, Rep. 27.

Chauvet, F., Dumont, T. & Basile, C., 2009. Structures and timing of Permian rifting in the central Oman Mountains (Saih Hatat), *Tectonophysics,* **475**(3-4), 563–574.

Christensen, N.I., 1996. Poisson's ratio and crustal seismology, *J. geophys. Res.,* **101**(B2), 3139–3156.

Christensen, N.I., 2004. Serpentinites, peridotites, and seismology, *Int. Geol. Rev.,* **46**(9), 795–816.

Christensen, N.I. & Smewing, J.D., 1981. Geology and seismic structure of the northern section of the Oman Ophiolite, *J. geophys. Res.,* **86**(B4), 2545–2555.

Crameri, F., Shephard, G.E. & Heron, P.J., 2020. The misuse of colour in science communication, *Nat. Commun.,* **11**(1), doi:10.1038/s41467-020-19160-7.

Darbyshire, F.A. & Lebedev, S., 2009. Rayleigh wave phase-velocity heterogeneity and multilayered azimuthal anisotropy of the Superior Craton, Ontario, *Geophys. J. Int.,* **176**(1), 215–234.

Deschamps, F., Lebedev, S., Meier, T. & Trampert, J., 2008. Azimuthal anisotropy of Rayleigh-wave phase velocities in the east-central United States, *Geophys. J. Int.,* **173**(3), 827–843.

Droste, H.H., 1997. Stratigraphy of the Lower Paleozoic Haima Supergroup of Oman, *GeoArabia,* **2**(4), 419–472.

El-Sharkawy, Amr, Meier, Thomas, Lebedev, Sergei, Behrmann, Jan H., Hamada, Mona, Cristiano, Luigia, Weidle, Christian & Köhn, Daniel, 2020. The Slab Puzzle of the Alpine-Mediterranean Region: Insights From a New, High-Resolution, Shear Wave Velocity Model of the Upper Mantle, *Geochemistry, Geophysics, Geosystems,* **21,** e2020GC008993, doi:10.1029/2020GC008993.

Forbes, G.A., Jansen, H. S.M. & Schreurs, J., 2010. Lexicon of Oman subsurface stratigraphy. Reference guide to the stratigraphy of Oman's Hydrocarbon basins, *GeoArabia,* 373 , Special Publication 5 by Gulf Petro Link.

Glennie, K.W., Boeuf, M.G.A., Hughes Clarke, M.W., Moody-Stuart, M., Pilaar, W. & Reinhardt, B.M., 1974. Geology of the Oman Mountains, *Koninklijk Nederlands Geologisch en Mijnbouwkundig Genootschap, Trans.,* **31**(1), 423.

Guilmette, C. *et al.*, 2018. Forced subduction initiation recorded in the sole and crust of the Semail Ophiolite of Oman, *Nat. Geosci.,* **11**(9), 688–695.

Hacker, B.R., Mosenfelder, J.L. & Gnos, E., 1996. Rapid emplacement of the Oman ophiolite: thermal and geochronologic constraints, *Tectonics,* **15**(6), 1230–1247.

Hansman, R.J., Ring, U., Scharf, A., Glodny, J. & Wan, B., 2021. Structural architecture and Late Cretaceous exhumation history of the Saih Hatat Dome (Oman), a review based on existing data and semi-restorable cross-sections, *Earth-Sci. Rev.,* **217,** doi:10.1016/j.earscirev.2021.103595.

Hansman, R.J., Ring, U., Thomson, S.N., den Brok, B. & Stübner, K., 2017. Late Eocene uplift of the Al Hajar Mountains, Oman, supported by stratigraphy and low-temperature thermochronology, *Tectonics,* **36**(12), 3081–3109.

Ji, S., Li, L., Motra, H.B., Wuttke, F., Sun, S., Michibayashi, K. & Salisbury, M.H., 2018. Poisson's ratio and auxetic properties of natural rocks, *J. geophys. Res.,* **123**(2), 1161–1185.

Jiménez-Munt, I., Fernàndez, M., Saura, E., Vergés, J. & Garcia-Castellanos, D., 2012. 3-D lithospheric structure and regional/residual Bouguer anomalies in the Arabia-Eurasia collision (Iran), *Geophys. J. Int.,* **190**(3), 1311–1324.

Kennett, B. & Engdahl, E., 1991. Traveltimes for global earthquake locations and phase identifications, *Geophys. J. Int.,* **105,** 429–65.

Kind, R., Kosarev, G.L. & Petersen, N.V., 1995. Receiver functions at the stations of the German regional seismic network (GRSN), *Geophys. J. Int.,* **121**(1), 191–202.

Knapmeyer-Endrun, B. & Krüger, F., the PASSEQ Working Group. 2014. Moho depth across the Trans-European Suture Zone from P- and S-receiver functions, *Geophys. J. Int.,* **197**(2), 1048–1075.

Langston, C., 1979. Structure under Mount Rainier, Washington, inferred from teleseismic body waves, *J. geophys. Res.,* **84**(B9), 4749–4762.

Laske, G., Masters., G., Ma, Z. & Pasyanos, M., 2013. Update on CRUST1.0—a 1-degree Global Model of Earth's Crust, in *Proceedings of the EGU General Assembly 2013,* held 7–12 April, 2013 in Vienna, Austria, id. EGU2013-2658.

Lebedev, S., Adam, J. M.-C. & Meier, T., 2013. Mapping the Moho with seismic surface waves: a review, resolution analysis, and recommended inversion strategies, *Tectonophysics,* **609,** 377–394.

Loosveld, R. J.H., Bell, A. & Terken, J. J.M., 1996. The tectonic evolution of interior Oman, *GeoArabia,* **1**(1), 28–51.

Manghnani, M.H. & Coleman, R.G., 1981. Gravity profiles across the Samail Ophiolite, Oman, *J. geophys. Res.,* **86**(B4), 2509–2525.

Mechie, J., Ben-Avraham, Z., Weber, M.H., Götze, H.-J., Koulakov, I., Mohsen, A. & Stiller, M., 2013. The distribution of Moho depths beneath the Arabian plate and margins, *Tectonophysics,* **609**(0), 234–249.

Moraetis, D., Mattern, F., Scharf, A., Frijia, G., Kusky, T.M., Yuan, Y. & El-Hussain, I., 2018. Neogene to Quaternary uplift history along the

Downloaded from https://academic.oup.com/gji/article/231/2/817/6609440 by CNRS user on 16 March 2023

passive margin of the northeastern Arabian Peninsula, eastern Al Hajar Mountains, Oman, *Quater. Res.,* **90**(02), 418–434.

Nicolas, A., Boudier, F. & Ildefonse, B., 1996. Variable crustal thickness in the Oman ophiolite: Implication for oceanic crust, *J. geophys. Res.,* **101**(B8), 17 941–17 950.

Nicolas, A., Boudier, F., Ildefonse, B. & Ball, E., 2000. Accretion of Oman and United Arab Emirates ophiolite – discussion of a new structural map, *Mar. Geophys. Res.,* **21,** 147–180.

Ninkabou, D., Agard, P., Nielsen, C., Smit, J., Gorini, C., Rodriguez, M., Haq, B., Chamot-Rooke, N., Weidle, C. & Ducassou, C., 2021. Structure of the offshore obducted Oman margin: emplacement of Semail ophiolite and role of tectonic inheritance, *J. geophys. Res.,* **126,** e2020JB020187.

Ravaut, P., Bayer, R., Hassani, R., Rousset, D. & Yahya'ey, A.A., 1997. Structure and evolution of the northern Oman margin: gravity and seismic constraints over the Zagros-Makran-Oman collision zone, *Tectonophysics,* **279**(1–4), 253–280.

Rickards, B.R., Booth, G.A., Paris, F. & Heward, A.P., 2010. Marine flooding events of the Early and Middle Ordovician of Oman and the United Arab Emirates and their graptolite, acritarch and chitinozoan associations, *GeoArabia,* **15**(4), 81–120.

Rioux, M., Garber, J., Bauer, A., Bowring, S., Searle, M., Kelemen, P. & Hacker, B., 2016. Synchronous formation of the metamorphic sole and igneous crust of the Semail ophiolite: new constraints on the tectonic evolution during ophiolite formation from high-precision U–Pb zircon geochronology, *Earth planet. Sci. Lett.,* **451,** 185–195.

Rodgers, A.J., Walter, W.R., Mellors, R.J., Al-Amri, A. M.S. & Zhang, Y.-S., 1999. Lithospheric structure of the Arabian Shield and Platform from complete regional waveform modelling and surface wave group velocities, *Geophys. J. Int.,* **138**(3), 871–878.

Scharf, A., Mattern, F., Al-Wardi, M., Frijia, G., Moraetis, D., Pracejus, B., Bauer, W. & Callegari, I., 2021. The Geology and Tectonics of the Jabal Akhdar and Saih Hatat Domes, Oman Mountains, *Geol. Soc., Lond., Mem.,* **54,** doi: 10.1144/M54.

Scharf, A., Mattern, F., Moraetis, D., Callegari, I. & Weidle, C., 2019. Postobductional kinematic evolution and geomorphology of a major regional structure—the Semail Gap Fault Zone (Oman Mountains), *Tectonics,* **38**(8), 2756–2778.

Schreurs, G. & Immenhauser, A., 1999. West-northwest directed obduction of the Batain Group on the eastern Oman continental margin at the Cretaceous-Tertiary boundary, *Tectonics,* **18**(1), 148–160.

Scripps Institution of Oceanography, 1986. *Global Seismograph Network - IRIS/IDA (GSN),* International Federation of Digital Seismograph Networks, doi:10.7914/SN/II.

Searle, M.P., 2007. Structural geometry, style and timing of deformation in the Hawasina Window, Al Jabal al Akhdar and Saih Hatat culminations, Oman Mountains, *GeoArabia,* **12,** 99–130.

Searle, M.P., Warren, C.J., Waters, D.J. & Parrish, R.R., 2004. Structural evolution, metamorphism and restoration of the Arabian continental margin, Saih Hatat region, Oman Mountains, *J. Struct. Geol.,* **26**(3), 451–473.

Tavani, S., Corradetti, A., Sabbatino, M., Seers, T. & Mazzoli, S., 2020. Geological record of the transition from induced to self-sustained subduction in the Oman Mountains, *J. Geodyn.,* **133,** doi:10.1016/j.jog.2019.101674.

Vinnik, L., 1977. Detection of waves converted from p to SV in the mantle, *Phys. Earth planet. Inter.,* **15**(1), 39–45.

Warren, C.J., Parrish, R.R., Waters, D.J. & Searle, M.P., 2005. Dating the geologic history of Oman's Semail ophiolite: insights from U-Pb geochronology, *Contrib. Mineral. Petrol.,* **150**(4), 403–422.

Weidle, C., Agard, P., Meier, T., Ducassou, C. & El-Hussain, I., 2013. COOL (Crust of the Oman Ophiolite and its Lithosphere) seismic network, GEOFON Data Archive,.

Wessel, P., Luis, J.F., Uieda, L., Scharroo, R., Wobbe, F., Smith, W. H.F. & Tian, D., 2019. The Generic Mapping Tools Version 6, *Geochem., Geophys., Geosyst.,* **20**(11), 5556–5564.

Whitehouse, M.J., Pease, V. & Al-Khirbash, S., 2016. Neoproterozoic crustal growth at the margin of the East Gondwana continent – age and isotopic constraints from the easternmost inliers of Oman, *Int. Geol. Rev.,* **58**(16), 2046–2064.

Wiesenberg, L., Weidle, C., El-Sharkawy, A., Timko, M., Lebedev, S. & Meier, T., 2022. Measuring the phase of ambient noise cross correlations: anisotropic Rayleigh and Love wave tomography across the Oman Mountains, *Geophys. J. Int.,* in press, doi:10.1093/gji/ggac232.

Wittlinger, G., Farra, V., Hetényi, G., Vergne, J. & Nábělek, J., 2009. Seismic velocities in Southern Tibet lower crust: a receiver function approach for eclogite detection, *Geophys. J. Int.,* **177**(3), 1037–1049.

Woodcock, N.H. & Robertson, A. H.F., 1982. Stratigraphy of the Mesozoic rocks above the Semail Ophiolite, Oman, *Geol. Mag.,* **119**(1), 67–76.

Wyns, R., Béchennec, F., Le Métour, J. & Roger, J., 1992. Geological map of Tiwi, sheet NF40-8B, scale 1:100,000, with explanatory notes, Tech. rep., Directorate General of Minerals, Oman Ministry of Petroleum and Minerals.

Yamato, P., Agard, P., Goffé, B., Andrade, V.D., Vidal, O. & Jolivet, L., 2007. New, high-precision P–T estimates for Oman blueschists: implications for obduction, nappe stacking and exhumation processes, *J. Metamor. Geol.,* **25**(6), 657–682.

Yuan, X., Kind, R., Li, X. & Wang, R., 2006. The S receiver functions: synthetics and data example, *Geophys. J. Int.,* **165**(2), 555–564.

Zhu, L. & Kanamori, H., 2000. Moho depth variation in southern California from teleseismic receiver functions, *J. geophys. Res.,* **105**(B2), 2969–2980.

APPENDIX: STATION TABLE

Downloaded from https://academic.oup.com/gji/article/231/2/817/6609440 by CNRS user on 16 March 2023

Table A1. Table of seismic stations used in this study, including Moho Depths and crust-average V_P/V_S ratios. Asterisk marks V_P/V_S at stations between the Semail Gap Fault and Ibra Zones where the values are not well constrained (see text and Fig. 10).

Station name	Longitude	Latitude	Elevation [m]	Moho depth [km]	V_P/V_S
COO01	58.7888	23.4151	17	34.5	1.84*
COO02	58.6888	23.2177	279	36.2	NaN
COO03	58.5288	23.1191	455	38.5	2.03*
COO04	58.3400	23.0859	685	39.7	1.97*
COO05	58.2340	22.8949	637	39.8	2.10*
COO06	58.1416	22.7809	546	39.3	1.96*
COO07	58.1336	22.6179	436	38.3	NaN
COO08	58.0312	22.4981	364	38.3	1.92*
COO09	57.7668	22.3875	299	39.0	1.92*
COO10	57.5925	22.2457	256	39.1	2.08*
COO11	58.3853	23.6030	22	35.7	NaN
COO12	57.9159	23.2736	435	39.0	1.97*
COO13	57.5365	22.8123	446	39.4	1.87*
COO14	57.0940	22.3183	248	37.8	NaN
COO15	57.8484	23.6967	17	37.2	NaN
COO16	57.4306	23.2706	616	40.1	1.66
COO17	56.8476	22.9219	567	39.1	1.85
COO18	56.6534	22.6785	288	39.0	NaN
COO19	57.4016	23.8204	27	38.5	NaN
COO20	56.8754	23.3827	548	39.4	1.79
COO21	56.4866	23.0293	316	39.1	NaN
COO22	56.8852	23.9251	158	39.5	1.71
COO23	56.5300	23.5777	548	39.5	1.81
COO24	56.2240	23.3219	283	39.3	1.64
COO25	56.5658	24.5439	21	40.1	NaN
COO26	56.2185	24.0300	758	39.8	1.74
COO27	55.9549	23.6171	265	39.1	1.61
COO28	56.2926	24.4480	503	39.7	1.73
COO29	55.8980	24.2367	360	38.9	1.66
COO30	58.3632	23.3442	428	37.4	1.77
COO31	59.0848	23.0216	20	34.0	1.85
COO32	58.7581	22.8347	526	36.2	1.78
COO33	58.4556	22.5523	420	36.0	1.86
COO34	58.2636	22.0729	235	37.3	NaN
COO35	59.2864	22.5885	530	34.3	NaN
COO36	59.1725	22.1361	161	33.6	1.80
COO37	58.7603	22.0989	264	35.0	1.86
COO38	59.8239	22.4341	16	34.2	NaN
COO39	59.6830	22.0867	16	33.4	1.86
COO40	59.4414	21.6855	61	33.2	1.70
COO41	57.1236	22.3112	254	37.8	NaN
COO42	58.2874	22.1428	247	37.1	1.94*
COO43	56.9608	22.2815	217	37.7	2.01*
COO44	56.5216	22.6902	249	39.2	1.80
COO45	57.5717	22.8102	442	39.5	NaN
COO46	58.1313	22.6180	436	38.3	NaN
COO47	59.8256	22.4233	40	34.2	NaN
COO51	58.7351	23.3191	211	35.2	2.05*
COO53	58.2459	23.0242	696	40.0	2.03*
ARQ	56.5219	23.3366	400	39.3	1.76
ASH	56.0583	24.6839	546	39.4	1.72
BAN	56.2996	25.9233	504	NaN	NaN
BID	58.1269	23.5211	200	37.2	1.87
BSY	57.1995	22.7446	450	39.1	1.81
HOQ	57.3109	23.5824	350	39.8	1.71
JLN	59.4108	22.1505	190	33.6	1.83
JMD	58.1035	22.3701	350	37.7	1.72
MDH	56.2983	25.2987	185	41.3	NaN
SMD	58.0492	23.0589	1000	39.7	1.88
SOH	56.5336	24.1342	100	40.0	1.86
WBK	58.9700	22.6100	450	34.3	1.83
WSAR	58.6307	23.2390	326	36.5	2.05*
UOSS	56.2042	24.9453	284	40.4	NaN
ASU	55.3292	24.6260	132	38.1	NaN
FAQ	55.5924	24.7453	203	38.6	1.66
HAT	56.1321	24.8257	340	39.9	1.70
NAZ	55.6618	24.9884	198	39.8	1.60

Downloaded from https://academic.oup.com/gji/article/231/2/817/6609440 by CNRS user on 16 March 2023